Application of Carbon Nanotubes for Photoacoustic Imaging Contrast Agent

Application of Carbon Nanotubes for Photoacoustic Imaging Contrast Agent

カーボンナノチューブの光音響イメージング増強剤への応用

Syahril Siregar

Graduate School of Biomedical Engineering

Tohoku University

A dissertation submitted for the degree of

Doctor of Biomedical Engineering

Sendai 2018

This dissertation is dedicated to

my dearest mother, Rubiah Harahap,

my father, Sofyan Siregar[1]*,*

my brother, Baginda Namora Parlindungan Siregar,

and my sister, Marini Siregar.

[1] 11 December 1954 - 5 December 2006

Acknowledgements

Alhamdulillah.[2] The completion of my doctoral studies over three years in Graduate School of Biomedical Engineering Tohoku University is the contribution of many people to whom I am very grateful to acknowledge. I would like to use this opportunity to thank them. First of all, I am grateful my supervisor, Professor Yoshifumi Saijo, for accepting me into his lab and to teach me the scientist attitude as well as an idea to find the novelty in the research. I would like to thank Professor Tatsuo Yoshinobu and Professor Yuji Matsuura as the committee members for evaluating my dissertation. I would like to express my gratitude to Dr. Ryo Nagaoka and Dr. Israr Ul Haq for teaching me a lot of basics idea of image processing and for helping me to use the photoacoustic microscopy in our laboratory. I would also thank to Kashiwagura-san, Ishikawa-san, Yaegashi-san, Shintate-san and Sato-san for helping me to setup the instruments in our lab. I want to express my appreciation to Dr. Muttaqin Yasin from IMRAM[3] Tohoku University and Abinubli-san from Graduate School of Agricultural Science Tohoku University for helping me to prepare and measure the UV-Vis spectra of carbon nanotubes samples.

I acknowledge partial financial support for research assistant from Japan Science and Technology Agency (JST) in Impulsing Paradigm Change

[2]Arabic word for all the praises and thanks be to Allah.
[3]Institute of Multidisciplinary Research for Advanced Materials

through Disruptive Technologies project (ImPACT) and Graduate School of Biomedical Engineering Tohoku University.

My sincere thanks go to Wakabayashi-san and Watanabe-san from Graduate School of Biomedical Engineering office for always helping me in administrative matters. Special thanks to the members of Saijo group; Sri-san, Maeda-san, Yokoshiki-san, Hirano-san, Ikeda-san, and Satou-san. I wanto to express my best regards to some professors in my master course who often give their outstanding support; Prof. Riichiro Saito, Dr. A.R.T. Nugraha, Dr. Pourya Ayria, and Dr. Muhammad Shoufie Ukhtary from Department of Physics, Tohoku University. I would like also to express my gratitude to the professors in my undergraduate course; Professor Rosari Saleh, Assoc. Professor Muhammad Azid Majidi, Assoc. Professor Supriyanto Suparno, and Assoc. Professor Dede Djuhana for their support. Lastly, I thank my family for their continuous support.

Abstract

The target of photoacoustic (PA) imaging does not always have high optical absorption. Consequently, the PA signal sometimes weak. Therefore, the PA contrast agents are required. This dissertation comprehends a study on the application of carbon nanotubes (CNTs) as PA imaging contrast agents. This study consists of three main parts. First, the developing of theoretical model of laser heating CNT to describe the temperature profile during laser irradiation. Our theoretical model of laser heating CNT declares that the maximum temperature during laser heating is proportional to the CNT diameter. Therefore, we suggest to use the larger diameter of the CNTs for PA imaging contrast agents. Second, the study on the PA properties of CNTs. Our experimental results confirm that CNTs have broad and high spectra in the visible and infrared regions. Accordingly, the high PA signal can be generated. Third, the investigation of filtering methods to remove the noise from the PA image. The proposed filtering methods are non-local means denoising and dictionary learning. Both filtering methods successfully enhanced the peak signal-to-noise ratio of the PA images. The proposed filtering methods are sensitive to the input parameters. So that, the suitable input parameters of proposed filtering methods will be comprehensively discussed.

Keywords:

carbon nanotubes, photoacoustic imaging, laser heating, non-local means denoising, dictionary learning

アブストラクト

光音響イメージングの観察対象は必ずしも吸光係数が高くないので光音響信号が弱いことがある。したがって、光音響イメージングの増強剤が必要である。本論文はカーボンナノチューブ (CNTs)の光音響増強剤への応用に関する研究について述べており、3つの部分から成っている。まず、レーザーによるCNTの加熱による温度プロファイルの理論モデル構築について述べている。本モデルにおいて、レーザーによる加熱中の温度はCNTの直径に比例することが示された。したがって、光音響増強には直径の大きなCNTを用いることが望まれる。次に、CNTsの光音響特性について述べている。実験的検討によりCNTは可視光および近赤外領域におよぶ広い光音響スペクトルを有し、強い光音響信号を発生することが示された。最後に光音響画像からのノイズ除去に関する検討について述べている。提案するフィルタリング手法はnon-local meansによるノイズ除去とdictionary learningで、それぞれのフィルタリング手法により光音響イメージングの信号 / 雑音比を高めることに成功した。本手法は入力パラメーターに鋭敏であり、適切な入力パラメーターを選択することが重要であることが示された。

List of abbreviations

AR-PAM Acoustic Resolution Photoacoustic Microscopy

CNT Carbon Nanotube

CT Computed Tomography

dB decibel

DMSO Dimethyl Sulfoxide

DWNT Double-Walled Carbon Nanotube

GCD Greatest Common Divisor

laser Light Amplification by Stimulated Emission of Radiation

MIP Maximum Intensity Projection

MRI Magnetic Resonance Imaging

MSE Mean Square Root

MWNT Multi-walled Carbon Nanotube

NIR Near-Infrared (wavelength 800 nm - 2500 nm)

NLMD Non-local means denoising

OCT Optical Coherence Tomography

OR-PAM Optical Resolution Photoacoustic Microscopy

PA Photoacoustic

PAM Photoacoustic Microscopy

PEG Polyethylene glycol

PET Positron Emission Tomography

PRF Pulse Repetition Frequency

PSNR Peak Signal-to-Noise Ratio

PTT Photothermal Therapy

PVA Polyvinyl Alcohol

SPECT Single Photon Emission Computed Tomography

SWNT Single-Walled Carbon Nanotube

Contents

List of Tables

Chapter 1

Introduction

In this chapter, the important purposes of the study, the motivation and organization of dissertation will be briefly discussed.

1.1 Purpose of the study

Medical imaging is the technique to obtain the image of organs or tissue in human body. Medical imaging is started from the discovery of X-rays by Wilhelm Conrad Roentgen[1]. Since the discovery of X-rays, the medical imaging technology has been dramatically growth up, for example, the researcher is able to make 4D computed tomography (CT) imaging of human body[2]. The medical imaging becomes powerful tools to diagnose the disease in the last century.

There are two electromagnetic radiation sources in the medical imaging; ionizing radiation and non-ionizing radiation. The electromagnetic spectrum can be seen in Figure1.1. The ionizing radiation is type of electromagnetic radiation that carries enough energy to release electron from atoms or molecules. The extreme ultraviolet, X-Rays, and Gamma rays are examples of ionizing radiation. The imaging modality using ionizing radiation are Rontgen, CT-scan, mammography, positron Emission Tomography (PET) and Single Photon Emission Computed Tomography (SPECT). The non-ionizing radiation is type of electromagnetic radiation that carries low en-

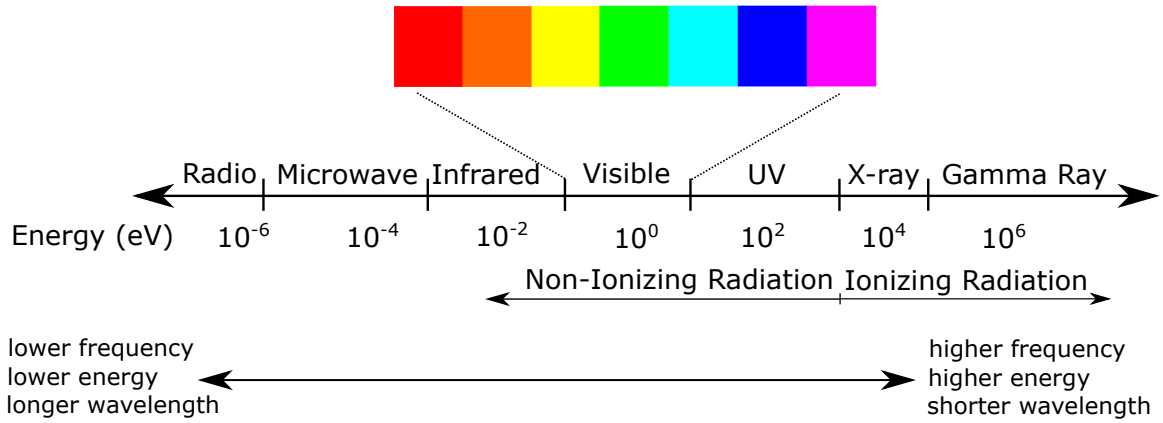

Figure 1.1: The electromagnetic spectrum.

ergy of photon which is not able to ionize atoms or molecules. The imaging technique using non-ionizing radiation are photoacoustic (PA) imaging, optical coherence tomography (OCT), multi-phonon microscopy, and confocal microscopy. The focus of this dissertation is PA imaging.

The PA imaging is new biomedical imaging modality to visualize the object based on the detected ultrasound generated when the object is irradiated by light[3]. The Phenomenon of generated ultrasound as a consequence of laser irradiation is called PA effect[4]. The PA imaging is able to combine the advantage of ultrasonic penetration depth and optical imaging resolution. The penetration depth of optical imaging is low due to the optical scattering in tissue while the penetration depth of ultrasound imaging is deeper than optical imaging. The high penetration depth in ultrasound imaging is caused by the scattering of ultrasound in tissue is weaker than optical scattering[5]. Consequently, the PA imaging provide better resolution for deep tissue than optical imaging[6]. The comparison between ultrasound imaging, PA imaging, and optical imaging can be seen in Table 1.1.

The laser in PA imaging is low intensity and non-ionizing laser[6]. Consequently, PA imaging is relatively safe in compared to another medical imaging using ionizing

Table 1.1: The comparison of imaging modalities.

Imaging modality	**Contrast**	**Depth (mm)**	**Resolution (mm)**
Ultrasonography	Acoustic impedance	∼60	∼300
Photoacoustic microscopy	Optical absorption	∼3	∼15
Photoacoustic tomography	Optical absorption	∼50	∼700
Optical coherence tomography	Optical scattering	∼2	∼10
Two photon microscopy	Fluorescene	∼0.5	∼3

radiation[7]. The PA imaging typically uses a green laser (532 nm) to irradiate the object [8]. Commonly, PA imaging can be used to obtain the image of skin, superficial organs, breast cancer, and small animal imaging[6].

The generated PA signal sometimes weak since not all of the target is a good light-absorber material. The typical raw PA image can be seen in Figure1.3. Consequently, the contrast agents materials are required in order to enhance the contrast of PA images. The contrast agents materials should be good light-absorber materials. The ability of materials to absorb light can be evaluated from the optical absorption spectra.

The contrast agent of PA imaging is also can be used for photothermal cancer treatment (PTT), since the PTT is also the application of laser-tissue interaction. In the case of PTT, the material agent is called heating agent. The combination of diagnostic and therapy is called theranostics. Consequently, the material agents in the both cases can be defined as theranostics agents.

Several materials for PA imaging contrast agents were proposed from previous works, such as gold nanoparticles and carbon based materials as shown in Table 1.2. The gold nanoparticles were commonly used as PA imaging contrast agents. Agarwal *et al.* reported that by using gold nanorod as PA imaging contrast agents, the contrast between targeted tissue and nontargeted tissue will be enhanced in an *in vitro* experiment[9]. Pai-Chi-Li *et al.* also reported the efficacy of using gold nanorod

as PA imaging contrast agents in multiple targets[10].

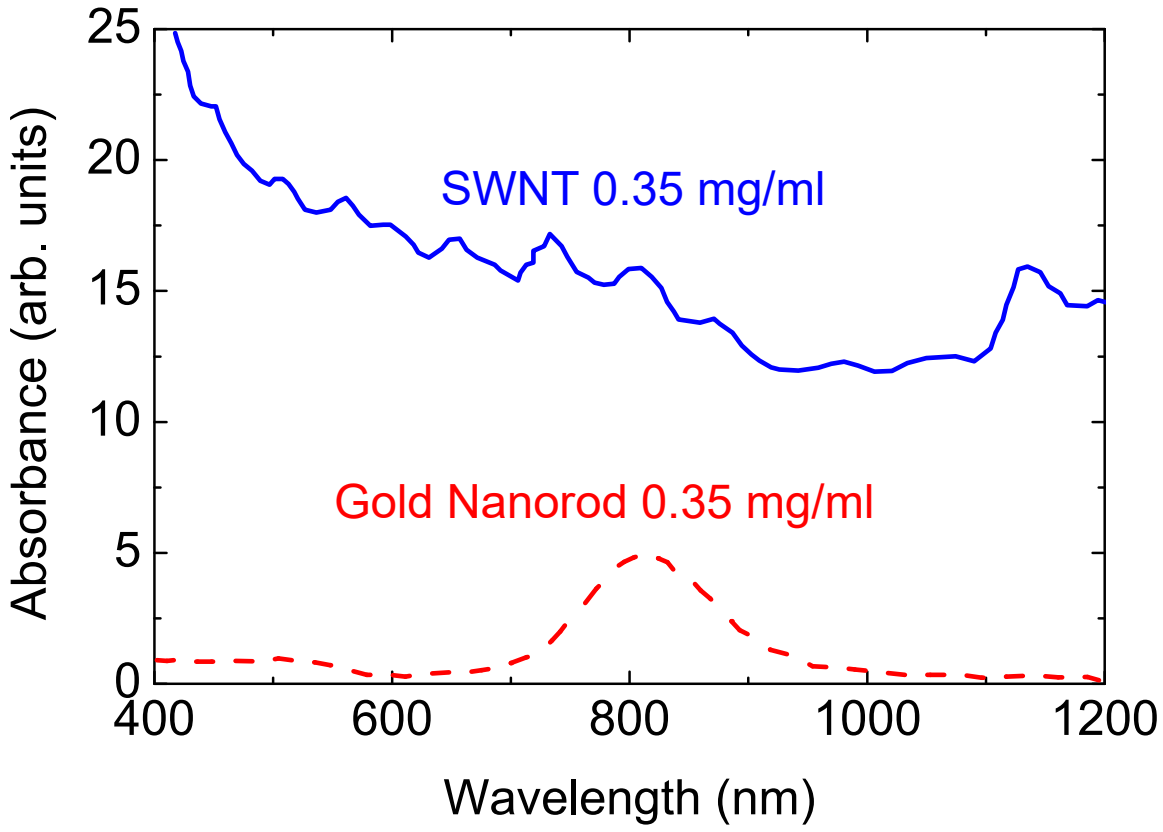

Figure 1.2: The absorption spectra of gold nanorod and SWNT on the same concentration, data are adapted from reference[11]. The absorption spectra of SWNT is a three-fold higher than gold nanorod at 808 nm[11].

Even though the gold nanorod is successfully applied as PA imaging contrast agents, the absorption spectra of gold nanorod is only third of single-walled carbon nanotubes (SWNTs) at 808 nm[11]. The comparison of gold nanorod and SWNTs spectra can be seen in Figure 1.2. Therefore, the SWNTs will produce PA signal stronger than gold nanorod. The peak position of gold nanoparticles is specific and narrow in the 750 nm – 850 nm. Consequently, the specific wavelength of laser is required. In the case of SWNTs, the absorption spectra is very broad so the wavelength of laser can be varying in the visible-infrared light. Moreover, the price of gold nanoparticles is also economically more expensive than CNTs. In the present re-

Table 1.2: The contrast agents for photoacoustic imaging.

No	Contrast agents	Size (nm)	Peak absorption (nm)
1	Gold nanorod[9]	40 - 60	650 - 1100
2	Gold nanosphere[12]	2 - 60	520 - 540
3	Gold nanocluster[13]	50 -100	700 - 900
4	Gold nanocages[14]	40	800
5	Gold nanoshells[15]	50-500	700 - 1100
6	Graphene Oxide[16]	0.8 - 1.2	232
7	Graphene nanosheets[17]	10 - 14	808
8	Functionalize Fullerenes[18]	100	650 - 750
9	Carbon nanotubes[19, 20]	5 - 300 nm	500- 600 and 690 - 800

search, we would like to investigate the CNTs for theranostics agents as an alternative to gold nanoparticles.

This dissertation proposes to use carbon nanotubes (CNTs) as potential candidate of the PA imaging contrast agents because CNTs have broad and high optical absorption in the visible and infrared regions[21, 22]. The penetration of infrared light into tissue are deeper than visible light[23, 24]. Furthermore, the image of deep tissue can be obtained by using CNTs and infrared laser in PA imaging. Additionally, the diameter of CNTs is relatively smaller than diameter of most gold nanoparticles, thus CNTs can be used to trat cancer cells which located in the specific place. Moreover, the thermal conductivity of CNTs is ten times higher than copper[25]. Therefore, based on its physical properties, CNTs is promised potential candidates for PTT heating agents and PA imaging contrast agents.

In this research, a theoretical model of laser heating CNTs to determine the best physical parameter of CNTs for PA imaging contrast agents will be developed. The theoretical model can be used to evaluate the relation between maximum temperature and diameter of CNTs during laser heating process. The proposed theoretical model of laser heating CNT is constructed based on the heat conduction equation which is the second order of partial differential equation.

This dissertation also investigates the PA properties of CNTs, by evaluating the

rise in temperature when the CNT is radiated by laser. This research uses green laser to evaluate the laser heating effect. The enhancement of PA signal is evaluated by comparing the image of CNT and red ink under PA microscopy.

The raw images of PA imaging are contaminated by noise due to some parameters such as laser induced components, transducer dimension, and less precise of time delay for PA wave. The typical noisy PA images can be seen in Figure1.3. In this research, the noise is assumed to be random noise. The noise degrade the size and shape of the object in the image, which inappropriate for diagnostic imaging. The noisy PA images possibly describe the wrong physical quantity, such as the size of blood vessel, and the region of interest. Thus, image processing to remove the noise is desperately required. The process to remove noise from the noisy image is called denoising process. Denoising process has very important role in medical image processing.

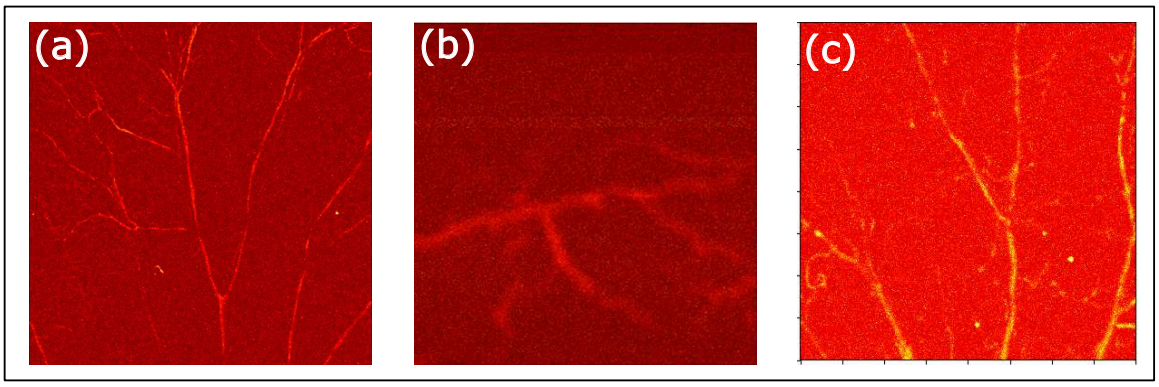

Figure 1.3: The raw images of PA imaging. (a) *In vivo* mice ear, (b) *in vivo* mice brain, (c) *in vivo* mice at different position with image (a), the raw images of PA imaging are low contrast and contaminated by noise.

This dissertation proposes two noise removal methods; non-local means denoising (NLMD) and dictionary learning methods. In order to apply the proposed noise removal methods, the best input parameters should be determined. Blurry image can be obtained by selected wrong input parameters. Furthermore, this dissertation also investigate the best input parameters of proposed noise removal methods. The CNTs

are used to produce the free noise image. Free noise image is used as synthetic data to investigate the enhancement of image quality after applying proposed denoising method.

Last but not least, the animal experiments in this dissertation were approved by Ethical Committee Review Board of Tohoku University.

As a summary, there are three main parts of the purposes of the study. First, the developing of a theoretical model of laser heating CNTs to obtain the suitable physical parameters of CNTs. Second, the experimental investigation of using CNTs as PA imaging contrast agents evaluated by PA properties. Third, the proposed noise removal methods in PA imaging with the suitable information about the input parameters.

1.2 Organization

This dissertation is organized into eight chapters. In the chapter 1, the purpose of the study and the organization of the dissertation are explained. In chapter 2, the basic of PA effect, PA imaging and the specification of the PA imaging system used in this research are introduced. The basics physical properties of CNTs such as electronics properties and optical properties will be reviewed in chapter 3. The usage of CNTs in biomedical engineering research will be reviewed in Chapter 3. The sample characterization of CNTs is also explained in Chapter 3. The theoretical model of laser heating CNTs will be explained in chapter 4. The proposed theoretical model can be used to obtain the temperature profile of CNTs and its surrounding tissue during laser irradiation process. The temperature profile is useful to determine the suitable physical parameters of CNTs for PA imaging contrast agents as well as PTT heating agents using CNTs. In Chapter 5, the PA properties of CNTs, the absorption spectra and *in vitro* experiments using PA imaging are explained. Several

denoising methods in PA imaging will be explained in the chapter 6 and chapter 7. In the chapter 6, the denoising method using non-local means denoising will be discussed. In the chapter 7, the denoising method using dictionary learning, a branch of machine learning will be explained. Finally, in the chapter 8, The summary and the conclusions of the dissertation will be given.

Chapter 2

Basics of photoacoustic imaging

In this chapter, the basics of photoacoustic effect and photoacoustic imaging will be reviewed. The theoretical background, the types of PA imaging system and also the image reconstruction method are given in this chapter.

2.1 Photoacoustic effect

Photoacoustic (PA) imaging or optoacoustic imaging is biomedical imaging modality based on PA effect. PA effect is the production of sound by means of light[4]. The PA effect is invented by Alexander Graham Bell on 1880[4, 26]. Thereafter, the PA research small development took place until the development of laser in 1960s[27] which provided coherence and high power light that many PA application need[28].

The early application of PA effect is the PA spectroscopy. The PA spectroscopy is used to investigate the optical properties of materials such as gas, solid and liquid[29]. PA spectroscopy is powerful tools to obtain the optical properties of opaque materials[30]. The PA spectroscopy is still used until now. Recently, it is used to detect the concentration of gas even in the part per trillion level[31].

The physics behind the PA spectroscopy is that some of the light is absorbed by materials, causing the temperature of materials increased. The suddenly change of temperature enhances the local pressure. Then, the pressure is propagating as

ultrasonic wave, which is called PA wave. The PA wave can be detected by using ultrasound transducer. The typical produced ultrasound frequency is 50 MHz.

2.2 Theoretical background of photoacoustic effect

In this subsection, the theoretical background of PA effect will be explained. The materials are adapted from "Biomedical Optics: Principles and Imaging" by L.V. Wang and H.I Wu[26].

The PA imaging use nanosecond pulse laser. Consequently, the laser heating is the time dependent physics problem. There are two important time variables in the laser heating process; thermal relaxation time and stress relaxation time.

The Thermal relaxation time is the duration of time needed for heat to diffuse on the distance (d). The thermal relaxation time is defined as

$$\tau_{th} = \frac{d_c^2}{\alpha_{th}}, \tag{2.1}$$

where d_c and α_{th} respectively are characteristic dimension of the heated region (m) and thermal diffusivity (m^2/s). The typical thermal diffusivity of soft tissue is in the order of 10^{-1} mm^2/s[32].

The stress relaxation time (τ_s) is defined as ratio between dimension of heated (d_c) region and the speed of sound (v_s) in the heated region. The stress relaxation time is given by

$$\tau_s = \frac{d_c}{v_s}. \tag{2.2}$$

The typical speed of sound in the tissue is ($\sim$1500 m/s)[33]. Normally, the stress relaxation time is much smaller than thermal relaxation time. Generally, the stress relaxation time is the range few nanoseconds. That is the reason why a nanoseconds laser is used in PA imaging. By comparing both times and the pulse-width of laser we can predict the physical phenomena. If the the pulse-width of laser is smaller

than τ_{th}, the laser excitation is classified to be thermal confinement and the heat conduction can be neglected. If the pulse-width of laser is much smaller than τ_s, the laser excitation can be categorized as in stress confinement and stress propagation can be neglected.

The fractional volume expansion ($\frac{dV}{V}$) is defined in equation(2.3). In the PA imaging, the laser excitation is satisfying thermal and stress confinements. Consequently, the fractional volume is zero.

$$\frac{dV}{V} = -\kappa p + \beta T, \tag{2.3}$$

$$0 = -\kappa p + \beta T,$$

$$T = \frac{\kappa p}{\beta}. \tag{2.4}$$

According to equation(2.4), the rise in pressure (p_0) due to laser heating can be written as

$$p_0 = \frac{\beta T}{\kappa}, \tag{2.5}$$

$$= \frac{\beta}{\kappa \rho C_V} \eta_{th} A_e, \tag{2.6}$$

where β and κ respectively are thermal coefficient of volume expansion and isothermal compressibility. A_e and η_{th} respectively denote the specific optical absorption ($\mathrm{J/m^3}$) and the efficiency of light converted into heat, with relation $T = \frac{\eta_{th} A_e}{\rho C_V}$. The isothermal compressibility (κ) can be defined as

$$\kappa = \frac{C_p}{\rho v_s^2 C_V}. \tag{2.7}$$

The Gruneisen parameter is a dimensionless parameter to describe anharmonic properties of solid[34]. It is also corresponds to the relation of rise in pressure to the

optical energy. The Gruneisen parameter can be defined as

$$\Gamma = \frac{\beta}{\kappa\rho C_V}, \tag{2.8}$$

$$= \frac{\beta v_s^2}{C_P}, \tag{2.9}$$

where $C_{V/P}$ is heat capacity at the constant volume or constant pressure. The Gruneisen parameter of water can be estimated by the empirical formula[26, 35] and is given by

$$\Gamma(To) = 0.0043 + 0.0053T_0, \tag{2.10}$$

where T_0 is the temperature in Celcius. In the case of soft tissue or breast tumor, the Gruneisen parameter is approximated as a constant around 0.24[36]. By substituting equation(2.8) into equation(2.6), the rise in pressure can be simplified as

$$P_0 = \Gamma\eta_{th}A_e, \tag{2.11}$$

$$= \Gamma\eta_{th}\mu_a F, \tag{2.12}$$

where μ_a and F respectively are optical absorption coefficient and the optical fluence ($\mathrm{J/cm^2}$). The relation is $A_e = \mu_a F$. According to equation(2.12), the gradient of pressure in PA phenomenon is affected by temperature rise, optical absorption coefficient, optical fluence, and the efficiency of light converted into heat. If we want to enhance the PA signal, we should control the affected parameters.

2.2.1 Photoacoustic wave equation

The PA wave is following the generalized wave equation. The generalized PA wave equation is defined as[37]

$$\nabla^2 p(\vec{r},t) - \frac{1}{v_s^2}\frac{\partial^2}{\partial t^2}p(\vec{r},t) = -\frac{\beta}{C_p}\frac{\partial}{\partial t}H(\vec{r},t), \tag{2.13}$$

where $p(\vec{r},t)$ is the acoustic pressure at the position $\vec{r}$ and time t. v_s is sound speed, β is isobaric volume expansion coefficient, C_P is the heat capacity per unit mass and H is the heating function.

By applying Green's function and some mathematical procedures, the equation(2.13) can be solved. The solution is given by

$$p(\vec{r},t) = \frac{1}{4\pi v_s^2}\frac{\partial}{\partial t}\left[\frac{1}{v_s t}\int d\vec{r'} p_0(\vec{r'})\delta\left(t - \frac{|\vec{r}-\vec{r'}|}{v_s}\right)\right], \tag{2.14}$$

where the heating source is assumed to be delta function (one pulse).

2.2.2 A slab excited by delta-pulse

In this subsection, the example of pressure propagating in the slab according to equation(2.14) will be explained. The schematic diagram of the slab can be seen in Figure2.1(b). There are three conditions exist in a slab excited by delta-pulse case;

1. $v_s t < z - d/2$, which means the spherical cell does not touch the the slab, so $p(z,t) = 0$.

2. $z - d/2 \leq v_s t \leq z + d/2$, which means the spherical cell intersects the edge of the slab at polar angle θ, by using equation(2.14), we can obtain the pressure $p(z,t) = p_0/2$.

3. $v_s t > z + d/2$, most part of the spherical shell intersects with slab, $p(z,t)$, $p(z,t) = 0$.

Based on three conditions above, the initial pressure distribution can be written as,

$$p_0(z) = p_0 U\left(z + \frac{d}{2}\right) U\left(-z + \frac{d}{2}\right), \tag{2.15}$$

where U is the Heaviside function. The distribution of pressure at any time can be expressed as

$$p(z,t) = \frac{1}{2}p_0(z - v_s t) + \frac{1}{2}p_0(z + v_s t). \tag{2.16}$$

The results of pressure propagation in the slab can be seen in Figure2.1(a). Initially the partial pressure for both p_+ and p_- is $0.5p_0$ and the total pressure is p_0. Then, the pressure changes as a function of time.

In the case of finite-duration of pulse excitation of a thin slab, the PA pressure can be approximated to the Gaussian function, that is

$$S(t) = S_0 \exp\left[\frac{(t - to)^2}{s\sigma^2}\right] \tag{2.17}$$

where S_0 and σ respectively are peak power and the standard deviation. The plot of $S(t)$ can be seen in Figure2.2(b).

2.2.3 A sphere excited by delta-pulse

The pressure propagating in the sphere is also can be solved by using equation(2.14). The schematic diagram of delta-pulse excitation of sphere can be seen in Figure2.1(c). According to the solution of equation(2.14), two equal pressures wave are produced. These wave is originating from the surface of the sphere. The resultant of these pressure is described as a bipolar wave. The resultant of pressure as the function of time at $r = 2R_s$ is shown in Figure 2.2

2.3 Photoacoustic imaging

The dominance of optical absorption as the source of PA signal in human body and animals are red blood cells, hemoglobin (HbO_2)[38, 39, 40]. Generally, there are two types of hemoglobin; oxyhemoglobin and deoxyhemoglobin. The hemoglobin saturated with oxygen is called oxyhemoglobin while the hemoglobin desaturated with oxygen is called deoxyhemoglobin. Both hemoglobins absorb light strongly in the visible region, especially green region as shown in Figure 2.3. Consequently, PA imaging system uses a green laser with wavelength 532 nm. Previous work also

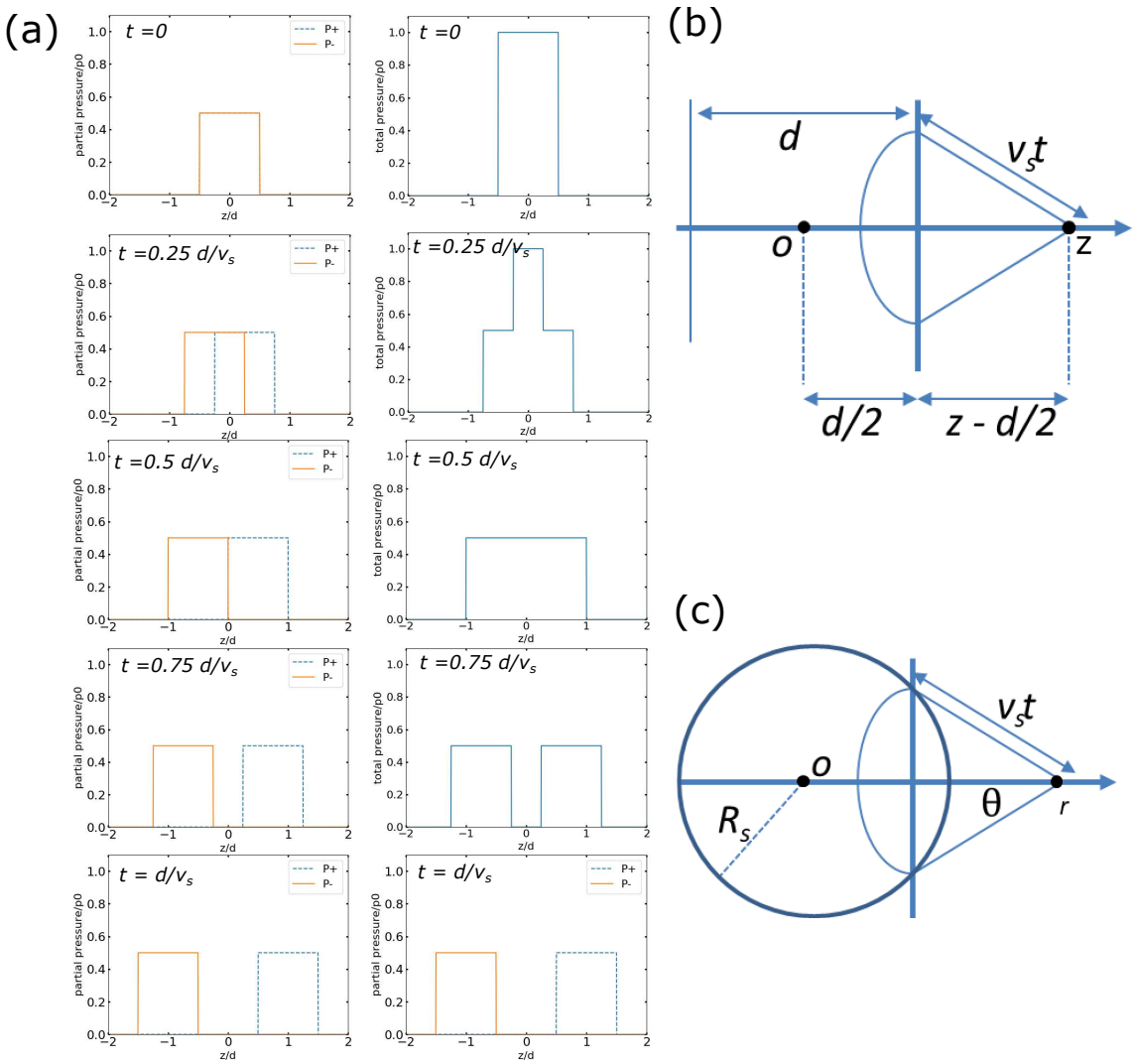

Figure 2.1: (a) Propagating pressure from heated slab in several times (b) schematic diagram for a slab, and (c) schematic diagram for a heated spherical object.

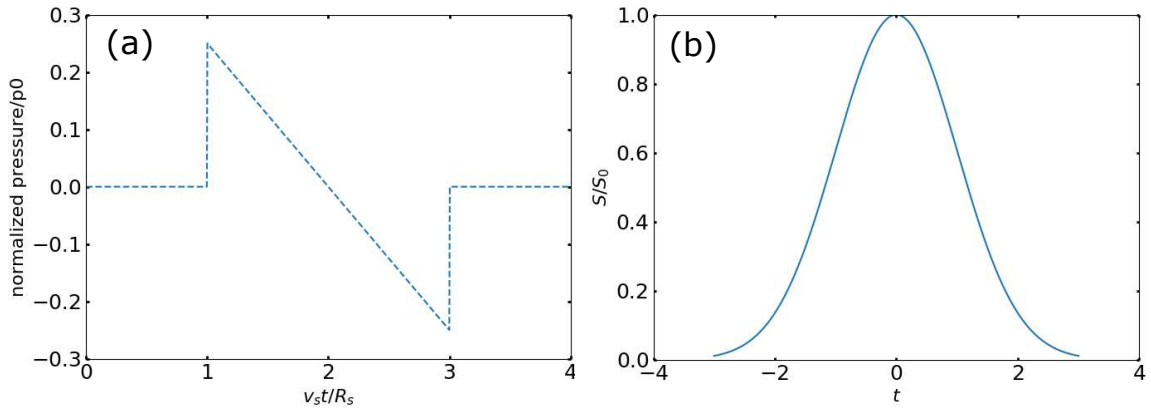

Figure 2.2: (a) The normalized pressure profile of heated sphere as a function of time. Pressure at $r = 2R_s$. (b) Photoacoustic pressure as a function of time.

mentioned that the red blood cells give high contrast relative to the its surrounding with factor 100 at 550 nm in PA imaging experiment[8].

Though, some PA imaging system use a near-infrared laser[43, 44, 45]. Water has low absorption spectra at green region but water has high absorption in the infrared region[42]. Consequently, water can be used as chromophore of PA imaging in the case of infrared laser[28]. In the case of infrared laser, melanin and lipids contribute as chromopores[46, 47]. Moreover by using multiple wavelength of laser to acquire image and applying the spectroscopic analysis, the concentration of the blood oxygen saturation can be obtained[38, 40, 48].

The mechanism of PA imaging is following several processes. First, hemoglobin molecules absorb the green light. The absorbed light causes the rise in local temperatures. The rise in temperature propagates causing the change of pressure creates the PA wave. The created PA wave is detected by using ultrasonic transducer.

PA Microscopy is the technique to obtain the PA image by mechanically scanning the focused ultrasound detector or the focused laser beam[28]. The image then formed directly by joining the single point measurement (A-line). The example of A-line can be seen in Figure 2.4. Generally, there are two types of PA microscopy; Acoustic Res-

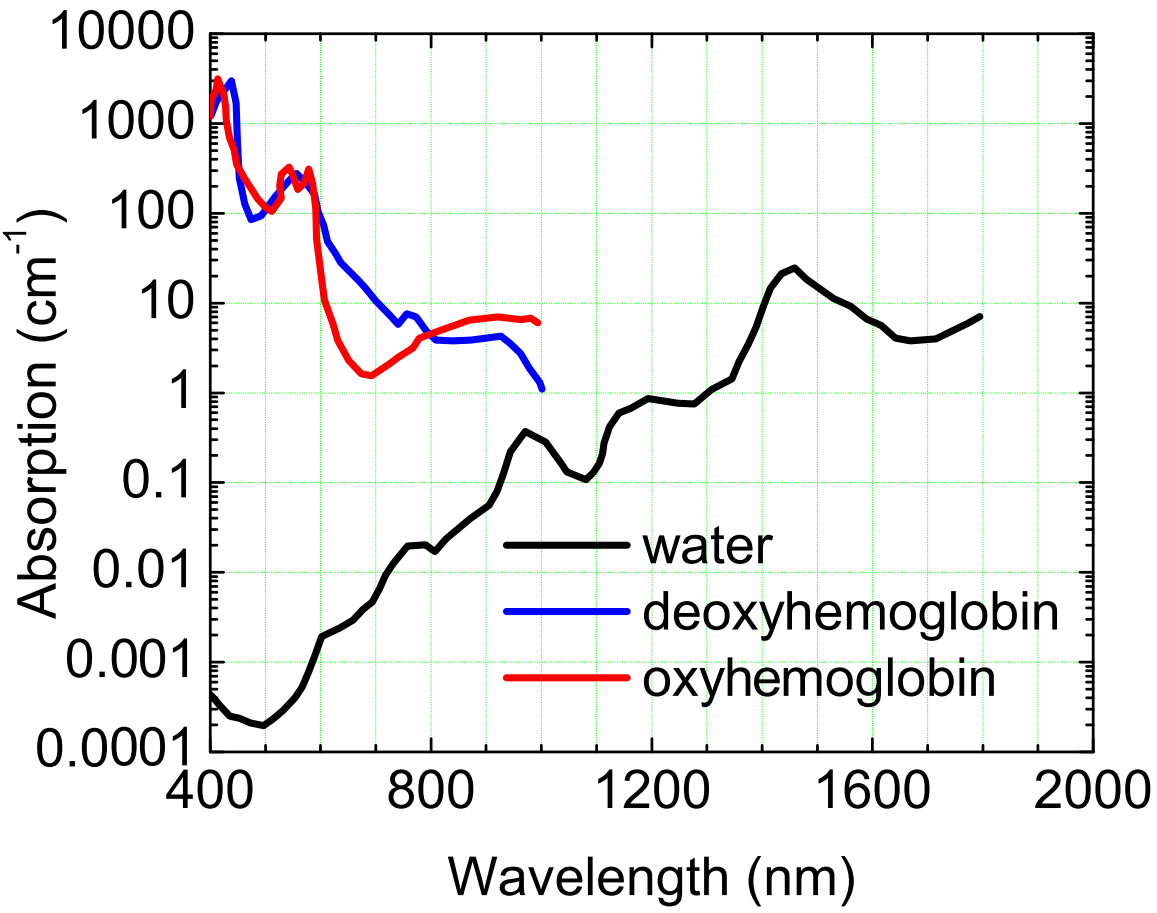

Figure 2.3: Absorption coefficient spectra of hemoglobins and water. Red line: deoxyhemoglobin, blue line: deoxyhemoglobin and black line: water. Data absorption spectra of hemoglobin were taken from reference[41] and data absorption spectra of water were taken from reference[42].

olution Photoacoustic Microscopy (AR-PAM) and Optical Resolution Photoacoustic Microscopy (OR-PAM). The AR-PAM uses a focused ultrasound detector while the OR-PAM uses a focused laser beam. The object on the both PAM system should be mediated by water since ultrasound wave propagates very slow in the air.

2.3.1 Acoustic resolution photoacoustic microscopy

AR-PAM is the PAM that use a mechanically translated or rotated focused transducer to acquire PA signal[28, 49, 50, 51]. In Figure 2.5(a), we show the schematic diagram of the AR-PAM system.

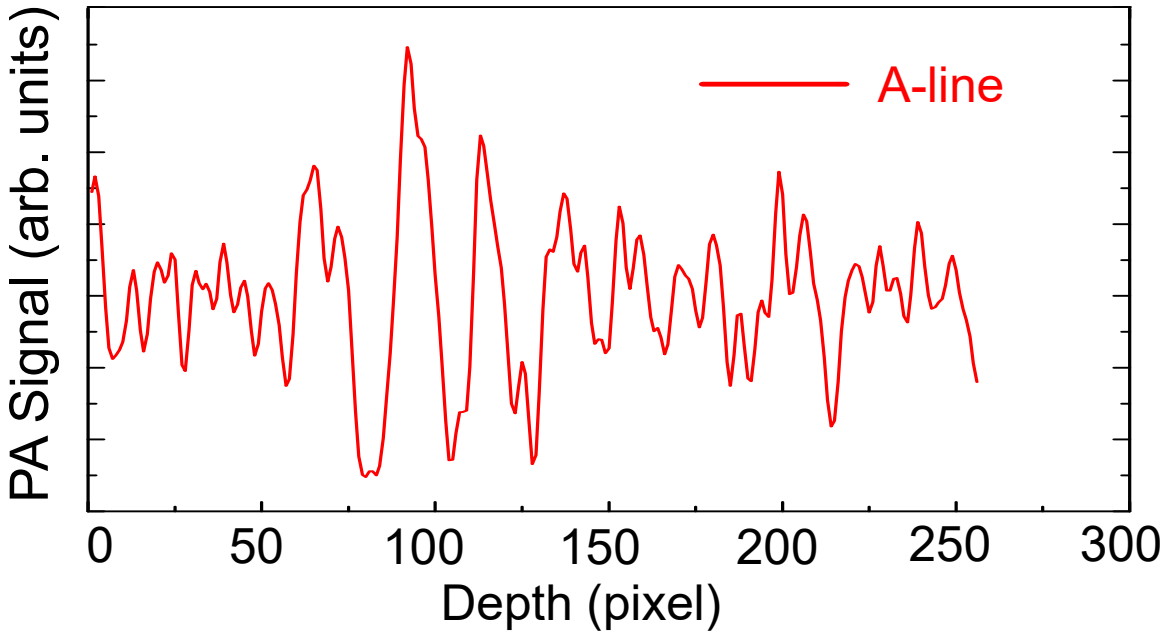

Figure 2.4: The example of A-line mode. A-line represents the depth profile.

The transducer and the laser beam are mechanically scanned to generate and to detect the PA wave at each step in order to acquire 3D image. The results are 2D collection data of A-lines, each A-lines has an information about depth profile. Consequently, the reconstruction tomography algorithm is not needed in AR-PAM. The depth of AR-PAM system can be enhanced to several centimeters[52].

The mechanism to acquire data of A-lines is given as follows. The object is irradiated by reflected light from two mirrors. This process creates the PA wave. The created PA wave is detected by a focused high-frequency ultrasound transducer. Then, the PA signal is amplified by amplifier. Computer is used to acquired the data and also for signal processing.

2.3.2 Optical resolution photoacoustic microscopy

The second type of PAM is OR-PAM in which optical focused laser beam control is used rather than acoustical control. The process to acquire data of A-lines is given as follows. First, the laser beam is collimated by a correction lens and focused by an

objective lens to minimize the focal spot in object. Typically, the diameter of focal spot is 5 μm [53]. This process generates PA wave. Then, the generated PA wave is reflected by silicon oil and prism to the ultrasound transducer. Computer is used to acquire data and reconstruct the image. The schematic diagram can be seen in Figure 2.5(b). The maximum detected depth in OR-PAM typically is 1 mm. This limitation is caused by the optical scattering.

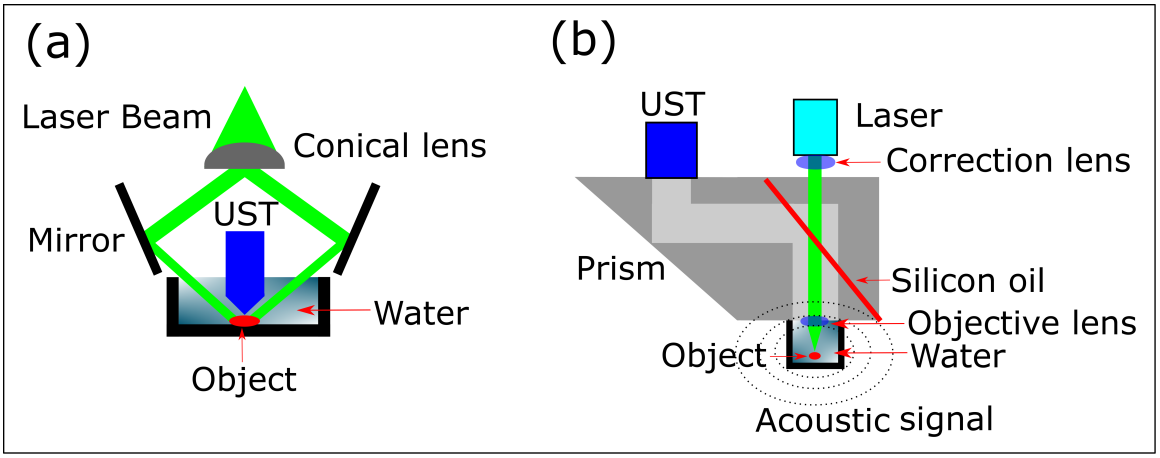

Figure 2.5: The schematic diagram of PAM. (a) AR-PAM, and (b) OR-PAM. UST is abbreviation of ultrasound transducer. The object and ultrasound transducer should be mediated by water or ultrasound gel because the ultrasound propagates very slow in air.

2.4 PA imaging system

We use the OR-PAM made in Micro Photo Acoustic, USA as our PA imaging system. The wavelength of the pulsed laser is 532 nm, the pulse duration is 8 ns and pulse repetition frequency (PRF) is 5 kHz. The ultrasound transducer with center frequency 20 MHz and sampling frequency 500 MHz is used to detect the PA wave. The maximum detected depth is 1 mm; deeper than this depth, the incident light from the laser will be scattered by tissue, as a consequence the signal become weak. The maximum axial and lateral resolutions are 15 and 5 μm.

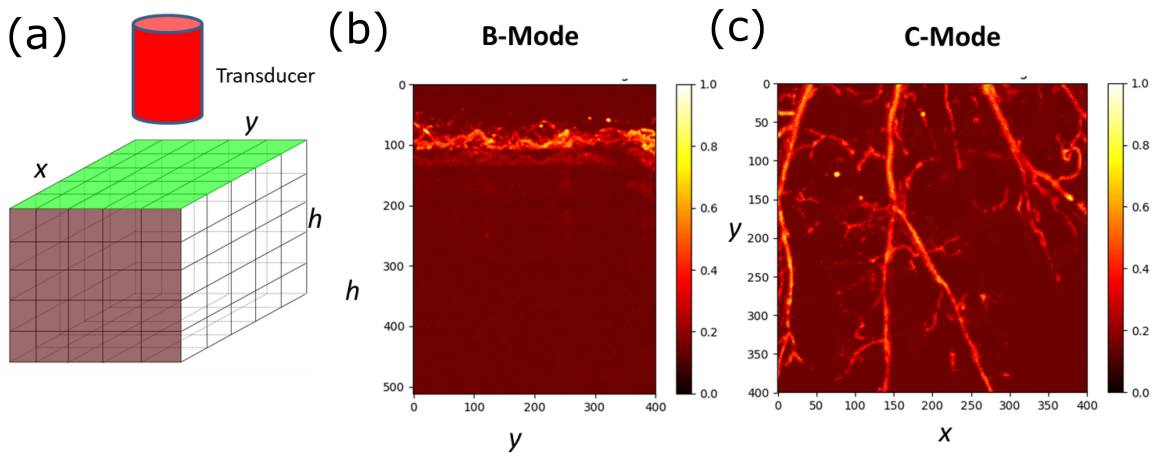

Figure 2.6: (a) The schematic diagram of 3D data, (b) B-Mode, and (c) C-Mode.

2.4.1 Image reconstruction

The acquired data from both PA microscopy are 3-dimensional data as shown in Figure 2.6(a). The view from $x-y$ plane is called the C-mode as shown in Figure 2.6(c). The projection if C-mode is using maximum intensity projection which mean taking the maximum pixel intensity for each layer of $x-y$ plane. The PA images in this dissertation are projected using maximum intensity projection C-mode.

The $x-h$ plane is called the B-mode as shown in in Figure 2.6(b). Actually, we can see the B-mode image for each layer of $x-h$ plane, but normally we also project the maximum intensity projection of the B-mode.

Chapter 3

Basics of carbon nanotubes

In this chapter, the basic physical properties of carbon nanotubes (CNTs) including the geometrical structure, electronic properties and optical properties will be reviewed. The usage of CNT in biomedical research also will be discussed.

3.1 Geometrical structure

CNTs structure is formed from graphene structure. However, the CNTs are discovered earlier than graphene. CNTs were discovered by Sumio Iijima in 1991 at NEC corporation, Japan[54]. In order to study the geometry of carbon nanotube, we have to understand the geometry of graphene. In this section, we will review the basic geometry of graphene and SWNT.

3.1.1 Graphene lattice

Graphene is the name of single layer carbon atoms (two-dimensional) in a honeycomb lattice[55]. Graphene was discovered by Andre Geim and Konstantin Novoselov in 2004 at the University of Manchester, England[56]. According to the lattice structure of graphene, every corner has an atom, with contributing one third and there is no atom in the center of the hexagon. Consequently, the unit cell consists of two distinct carbon atoms A and B, respectively represented by red and blue dots in Figure 3.1(a). The nearest-neighbor inter-atomic distance (a_{cc}) is 1.42 Å [57].

In Figure 3.1, we show (a) the unit cell of graphene and (b) the reciprocal lattice of graphene. The unit vectors of graphene in the x, y coordinates are given by

$$\begin{cases} \mathbf{a}_1 = \dfrac{\sqrt{3}a}{2}\hat{\mathbf{x}} + \dfrac{a}{2}\hat{\mathbf{y}}, \\ \mathbf{a}_2 = \dfrac{\sqrt{3}a}{2}\hat{\mathbf{x}} - \dfrac{a}{2}\hat{\mathbf{y}}, \end{cases} \tag{3.1}$$

where $\hat{\mathrm{x}}$ and $\hat{\mathrm{y}}$ are the unit vector in x and y directions of graphene layer and $a = \sqrt{3}\, a_{CC} = 2.46$ Å is the lattice constant of single graphene layer. The angle between a_1 and a_2 is 60°.

The reciprocal lattice vectors of graphene can be derived according to the following definition

$$\mathbf{a}_i \cdot \mathbf{b}_j = 2\pi\delta_{ij}, \tag{3.2}$$

where δ_{ij} is the Kronecker delta function. Therefore, the reciprocal unit vectors $\mathbf{b}_1$ and $\mathbf{b}_2$ are given by

$$\begin{cases} \mathbf{b}_1 = \dfrac{2\pi}{\sqrt{3}a}\hat{\mathbf{x}} + \dfrac{2\pi}{a}\hat{\mathbf{y}}, \\ \mathbf{b}_2 = \dfrac{2\pi}{\sqrt{3}a}\hat{\mathbf{x}} - \dfrac{2\pi}{a}\hat{\mathbf{y}}. \end{cases} \tag{3.3}$$

The angle between $\mathbf{b}_1$ and $\mathbf{b}_2$ are 120°.

3.1.2 Structure of SWNT

Based on the number of wall, there are three types of carbon nanotubes; single-walled carbon nanotubes, double-walled carbon nanotubes (DWNT), and multi-walled carbon nanotubes (MWNT) as shown in Figure 3.3(b). However, we will review the geometry of SWNT. SWNT are non-Bravais lattice. The unit cell of a SWNT is defined by two vectors: the translational vector $\mathbf{T}$ and the chiral vector $\mathbf{C_h}$.

The chiral vector $\mathbf{C_h}$ represent the circumference of the SWNT while the translational vector $\mathbf{T}$ represent the length of SWNT. The chiral vector can be formulated

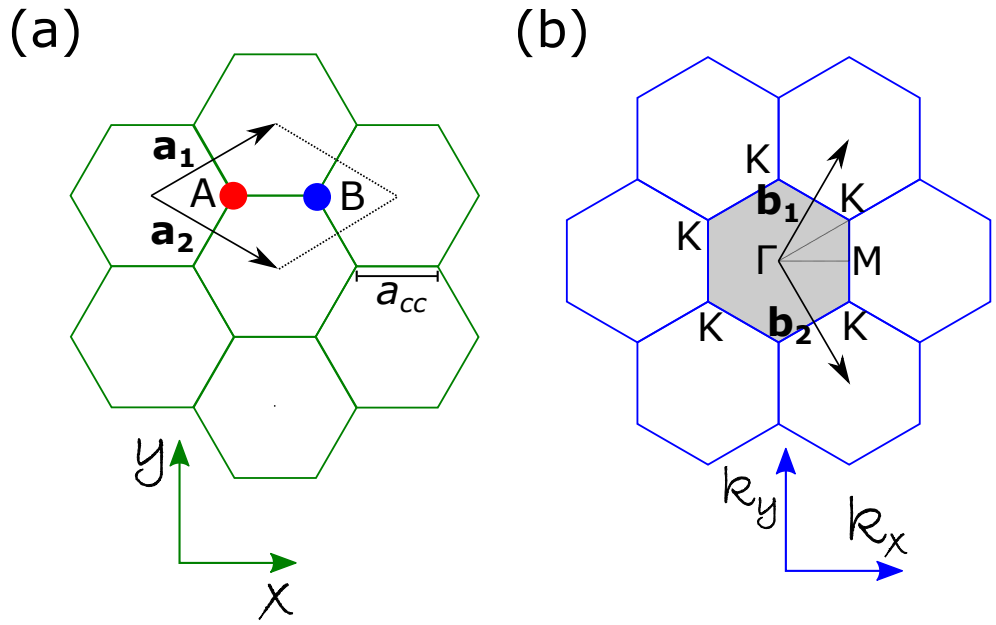

Figure 3.1: (a) The unit cell of graphene is shown as the dotted area. The blue and red circles represent two atoms in a unit cell of graphene. The unit vectors $\mathbf{a_1}$ and $\mathbf{a_2}$ are shown by arrows. (b) The reciprocal lattice of graphene. The reciprocal lattice vectors b_1 and b_2 are shown by arrows in the k_x and k_y coordinates. Important points in Brillouin zone are K, Γ, and M.

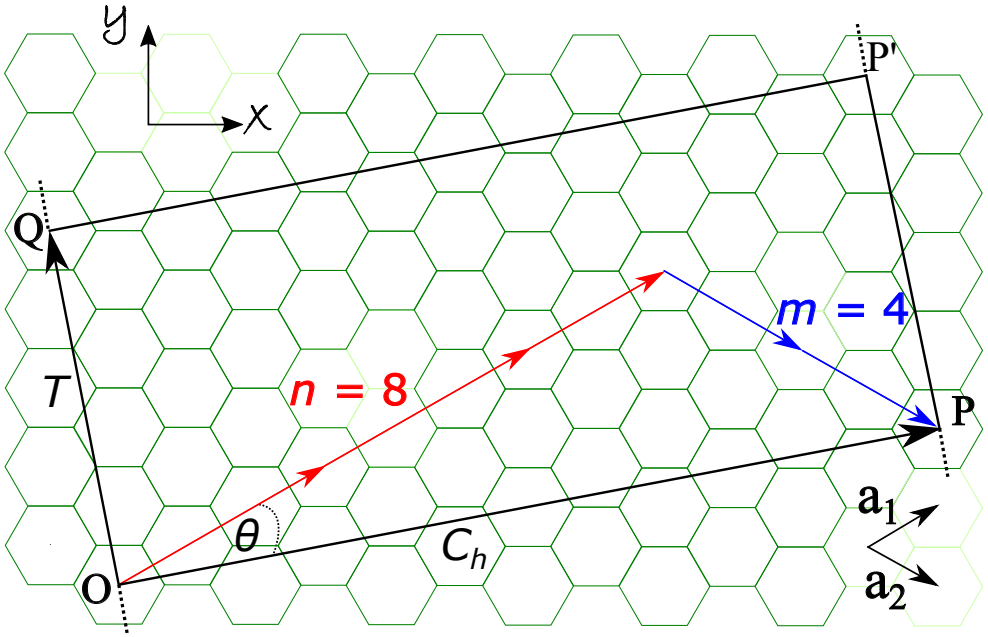

Figure 3.2: Geometry of (8,4) SWNT formed from graphene sheet with $\mathbf{a_1}$ and $\mathbf{a_2}$ are graphene unit vectors. The SWNT can be constructed by joining O to P and Q to P′. The translational and chiral vectors are denoted as $\mathbf{T}$ and $\mathbf{C_h}$.

in the terms of a_1 and a_2 as

$$\begin{aligned} \mathbf{C_h} &= n\mathbf{a_1} + m\mathbf{a_1}, \\ &\equiv (n, m), \end{aligned} \tag{3.4}$$

where $n > m$, $n > 0$ and $m \geq 0$. The magnitude of chiral vector $\mathbf{C_h}$ is the circumference of SWNT (L), can be formulated as

$$L = |\mathbf{C_h}| = a\sqrt{n^2 + m^2 + nm}. \tag{3.5}$$

The diameter of SWNT can be formulated from the circumference. The diameter d_{SWNT} is given by,

$$\begin{aligned} d_{SWNT} &= \frac{L}{\pi}, \\ &= \frac{a\sqrt{n^2 + m^2 + nm}}{\pi}. \end{aligned} \tag{3.6}$$

The angle between $\mathbf{C_h}$ and $\mathbf{a_1}$ is defined as chiral angle (θ). The chiral angle can be obtained by solving the angle between two vectors problem. The expression of chiral angle is

$$\theta = \cos^{-1}\left(\frac{2n + m}{2\sqrt{n^2 + m^2 + nm}}\right). \tag{3.7}$$

The translational vector $\mathbf{T}$ is perpendicular to the chiral vector $\mathbf{C_h}$ and can be formulated as

$$\mathbf{T} = t_1\mathbf{a_1} + t_2\mathbf{a_1} \tag{3.8}$$

where t_1 and t_2 are obtained by following the perpendicular condition $\mathbf{C_h} \cdot \mathbf{T} = 0$, t_1 and t_2 are

$$\begin{aligned} t_1 &= \frac{2m + n}{\mathrm{GCD}[(2m + n), (2n + M)]}, \\ t_2 &= -\frac{2n + m}{\mathrm{GCD}[(2m + n), (2n + M)]}, \end{aligned} \tag{3.9}$$

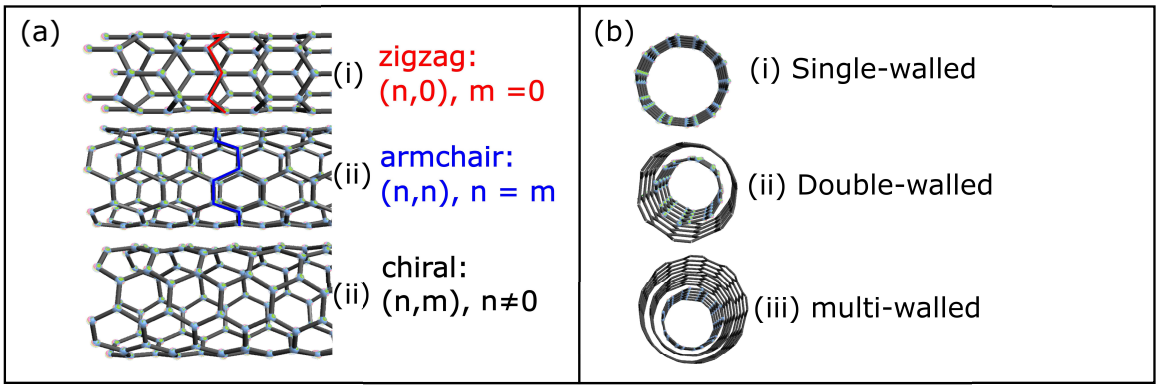

Figure 3.3: (a) Classification of SWNTs based on the chirality. (b) Classification of CNTs based on the number of walls.

where GCD is greatest common divisor. equation(3.9) is following GCD$(t1, t2) = 1$ condition. The length of SWNT (length of translation vector), $|\mathbf{T}|$ is given by

$$|\mathbf{T}| = \frac{L\sqrt{3}}{\mathrm{GCD}[(2m+n),(2n+M)]}. \tag{3.10}$$

The parameters of SWNT are shown in Figure3.2. The parameter (n, m) is normally used to classify SWNT. There are three types of SWNTs based on its chirality; zigzag, armchair and chiral as shown in Figure3.3(a).

3.2 Electronic properties

3.2.1 Electronic properties of graphene

The electronic structure of graphene can be calculated by using simple tigh binding approximation[57, 58]. Based on reference [57], the electronic structure of graphene can be written as

$$E^v(\mathbf{k}) = \frac{\varepsilon_{2p} + tw(\mathbf{k})}{1 + sw(\mathbf{k})}, \tag{3.11}$$

$$E^c(\mathbf{k}) = \frac{\varepsilon_{2p} - tw(\mathbf{k})}{1 - sw(\mathbf{k})}, \tag{3.12}$$

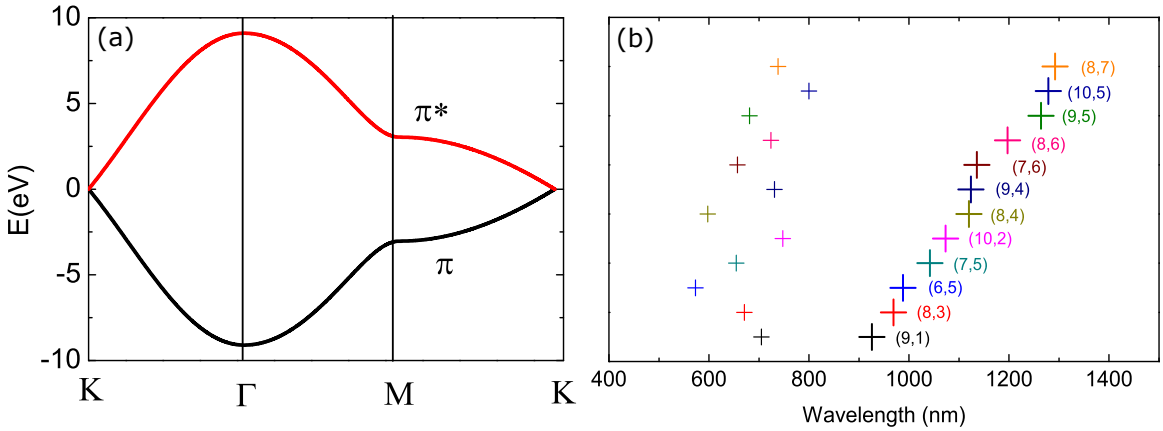

Figure 3.4: (a)The energy dispersion of graphene at the high symmetry points in Brillouin zone. Near the K point, the energy dispersion of graphene is linear.(b) The absorption spectra of several chiralities of SWNTs. Data are taken from Xiaomin Tu *et al.*[59].

where the band indexes c, v denote the conduction and valence bands, and $(t < 0)$, $(s > 0)$. $w(\mathbf{k})$ defined as

$$w(\mathbf{k}) = \sqrt{1 + 4\cos\left(\frac{\sqrt{3}}{2}k_x a\right)\cos\left(\frac{1}{2}k_y a\right) + 4\cos^2\left(\frac{1}{2}k_y a\right)}. \tag{3.13}$$

In the case of simple approximation, the several parameters become zero, $s = 0$ and $e_{2p} = 0$. In Figure3.4(a), we show the energy dispersion of graphene at high symmetry points. The conduction and valence bands touch each other without overlapping in the K point. Near the K point, the energy dispersion of graphene is linearly proportional to the $\mathbf{k}$ as shown in Figure3.4(a). Consequently, the electrons and holes in graphene have high mobility, which approved by high electrical conductivity[60].

3.2.2 Electronic properties of SWNT

The electronics properties of SWNT can be classified into two groups, metallic and semiconductor. The electronic properties of SWNT can be determined easily from the chirality.

$$\text{electronic properties} \begin{cases} \text{metalic}, & \text{if } n - m = 3i \\ \text{semiconducting}, & \text{otherwise} \end{cases} \tag{3.14}$$

3.3 Optical properties of carbon nanotubes

In this part, we will review the optical properties of carbon nanotubes based on the absorption spectra measured by using uv-vis spectroscopy. In the present research, the information about absorption spectra is very important since the peak position in absorption spectra demonstrates the suggested wavelength of laser for PA imaging.

In Figure 3.4(b), we show the peak positions of UV-Vis-NIR spectra of SWNTs for several chiralities, the numerical data is adapted from reference[59]. Generally, two peaks exist in UV-Vis-NIR spectra for each chirality, the stronger peak appears in the 900 nm–1300 nm around the second near-infrared (NIR) window and the weaker peak appear in the 500 nm − 800 nm (around the first NIR window).

3.4 CNT in biomedical engineering research

Over the decades, CNTs has received outstanding attention owing to its unique physical properties and the prospects for biomedical application[61, 62, 63]. The CNTs can be used as heating agents of photothermal therapy (PTT) to treat the cancer [64, 21, 65]. Previous work also mentioned that the CNT enhanced the photothermal destruction of tumor cells and protected the normal cells[64]. Zhuang Liu *et al.* investigated the function of CNT as drug delivery in tumor targeted medicine[66].

CNTs also widely used in the diagnostic imaging agents such as the contrast agents of fluorescence imaging[67, 19], micro PET[63], Raman imaging[68], MRI [69, 70] PA imaging [19], ultrasound imaging[71], and single photon emission computed tomography (SPECT)[72].

In the tissue engineering research, CNTs can be used for scaffold materials for osteoblast proliferation and bone formation[73, 74, 75] and artificial muscles[76]. Gene therapy also can be improved by using CNTs that support in the replacement of dam-

aged genes[77]. Some researchers also reported that CNTs can be used for biosensor to monitor concentration of glucose in the blood[78].

Despite the widely potential of CNTs in biomedical researches, some papers reported the CNTs can potentially cause adverse effect in the biological object because of their tiny size and extreme aspect ratio[79, 80]. However, another papers mentioned that the CNTs are safe to biological objects[81]. The small dosage of CNTs 40 μg/ml was reported safe in HeLa cells[82].

The biocompatibility issue in CNTs is related to the size, concentration, dosage, and defects[80]. As a conclusion, more study on the safety of CNTs is needed especially about the dosage, aspect ratio, and size of CNTs before injecting CNTs to human body.

3.5 Sample preparation of CNTs

The CNTs samples used in this study are commercially available CoMoCAT SWNT(6,5) powder. CNTs are insoluable in organics solvent including water[83, 84, 85, 86]. In order to use the CNTs in biomedical research, we have to dissolve the CNTs. In our sample preparations, we mixed 12 miligram powder of CNT with 12 gram of liquid polyethylene glycol (PEG)-400. We use PEG as solvent because PEG-modified CNTs have been successfully tested in biomedicine[87]. However, the CNT does not immediately dissolved in the PEG. We treated the samples with the ultrasonic wave for 2 hours by using sonicator, Branson Yamato 2510. The large amount of CNT was dissolved after sonicating process but some parts still in the powder phase.

Chapter 4

Laser heating carbon nanotubes

In this chapter, the theoretical model of laser heating CNTs based on the classical heat conduction equation will be discussed. The theoretical calculation is very important to determine the suggested specification of CNTs for PA imaging contrast agent as well as heating agents of PTT. Some materials in this chapter were published in the Nanomaterials with title "A Theoretical Model of Laser Heating Carbon Nanotubes"[88] and in the arXiv [89].

4.1 Introduction to model

The usage of CNTs in contrast agents of PA imaging is to increase the PA signal. The PA imaging is application of laser heating materials. The high PA signal can be produced by high gradient of temperature during laser irradiation. Correspondingly, the PA signal intensity proportional to the gradient temperature during laser irradiation. Consequently, temperature profile of contrast agents during laser irradiation is essential parameter.

The PTT is also application of laser heating process. The cancer cells can be destroyed by increasing its temperature to the 41–47 °C [90]. Furthermore, the PTT using heating agents should be able to increase the temperature of cancer cells at least up to 41–47 °C. This optimum temperature causes the cancer cells to become

hyperthermic and damaged due to the destitute of blood supply [91].

The objective of present work is to develop a simple theoretical model of laser heating CNT. Based on our model, we would like to calculate the temperature profile in CNT and cancer cells during laser heating process. Appropriately, the interface temperature between CNT and cancer cells can be determined.

Based on the solution of our model, we could suggest the effective specification of CNT for future cancer treatment. Our model possibly can be extended for the nanotube based materials, such double-walled and multi-walled CNTs. Our model also might be suitable for another application of laser heating nanotubes materials.

4.2 Theoretical model

The model of heat propagation in the cancer cells and CNT, during laser heating process by using classical heat conduction equation is developed. The CNT is represented by a solid cylinder model. This assumption is normal in the theoretical simulation of CNTs. For example, to investigate the the mechanical properties of CNTs[92], CNT is modeled by solid cylinder. The diameter of CNTs is very small and the density of atom is high especially for double-walled and multi-walled CNTs. Consequently, solid cylinder model is also reasonable.

In this model, the CNT is surrounded by cancer cells as a target as shown in Figure 4.1. The Radius of cylinder is denoted by a and the farthest considered distance (b) is 300 times radius of cylinder with its temperature (T_b) is the temperature of normal human body 37^{o}C.

We have several assumptions to simplify the problems . First, the length of cylinder is much greater than its diameter. This assumption is reasonable since previous work reported that the length-to-diameter ratio of CNTs can be more than 1000[93]. Correspondingly, the laser heating CNTs is only a function of radial distance. More-

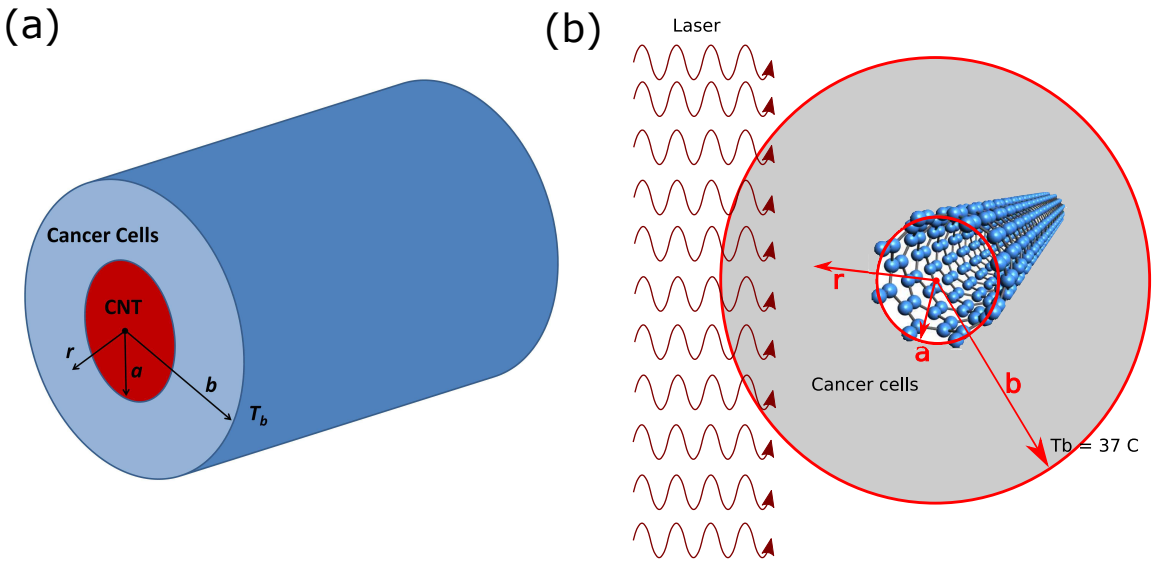

Figure 4.1: (a) Solid cylinder model. (b) The CNT at the center of cancer cells is heated by laser. The radius of of CNT is a.

over, the laser spot is also much greater than the dimension of CNT as a consequence, the angle dependence of laser heating process can be neglected.

According to the model, the laser heating process can be formulated by using heat equation. The heat equation is second order partial differential equation, and can be formulated as,

$$\rho_c c_c \frac{\partial T}{\partial t} = k_c \frac{1}{r}\frac{\partial}{\partial r}\left(r\frac{\partial T}{\partial r}\right) + q(r,t), \quad 0 < r < a, \tag{4.1}$$

$$\rho_t c_t \frac{\partial T}{\partial t} = k_t \frac{1}{r}\frac{\partial}{\partial r}\left(r\frac{\partial T}{\partial r}\right), \quad r > a, \tag{4.2}$$

where $\rho_{c,t}$ is the density of CNT,cancer cells, $k_{c,t}$ is the thermal conductivity of CNT,cancer cells, T is temperature, r is radial distance measured from the center of the nanotube as shown in Figure4.1. t is time and $q(r,t)$ is the heat source which representing the laser heating process.

For simplicity, we neglect the time dependence of temperature. Consequently, the temperature during the laser heating is only the function of radial distance. The

eqs.(4.1)-(4.2) become,

$$\frac{k_c}{r}\frac{d}{dr}\left(r\frac{dT}{dr}\right) + q(r) = 0, \quad 0 < r < a, \tag{4.3}$$

$$\frac{k_t}{r}\frac{d}{dr}\left(r\frac{dT}{dr}\right) = 0, \quad r > a. \tag{4.4}$$

Boundary and initial conditions are very important to solve the differential equation. The boundary and initial conditions in our model are given by,

$$\frac{dT}{dr} = 0, \quad \text{at } r = 0, \tag{4.5}$$

$$k_c\left(\frac{dT}{dr}\right)\Big|_{r=a_-} = k_t\left(\frac{dT}{dr}\right)\Big|_{r=a_+} \tag{4.6}$$

$$T(a_-) = T(a_+), \tag{4.7}$$

$$T = T_\infty\ (T_b) \ \text{ at } r \to \infty (r = b). \tag{4.8}$$

The temperature at the center of the cylinder during laser heating should be definable, as described in equation(4.5). equations.(4.6) and (4.7) show that the temperature inner and outer sides of cylinder must be continuous at the interface of cancer cells and the cylinder.

The heat source from laser heating can be defined as,

$$q(r) = (1 - R)I_0\alpha\exp(-\alpha z), \quad \text{with } z = a - r. \tag{4.9}$$

Where I_0 is the laser intensity, α is absorption coefficient of CNT, R is the reflectivity, and z is the depth, measured from the interface to the center of the cylinder. The heat source is the function of radial distance r. The heat source will be decayed as a function of depth measured from a surface. However, we neglect the exponential term and assuming the heat source is constant for simplicity. For several values of diameter of cylinder, the decayed is not very strong as shown in Figure 4.2(b). However, when

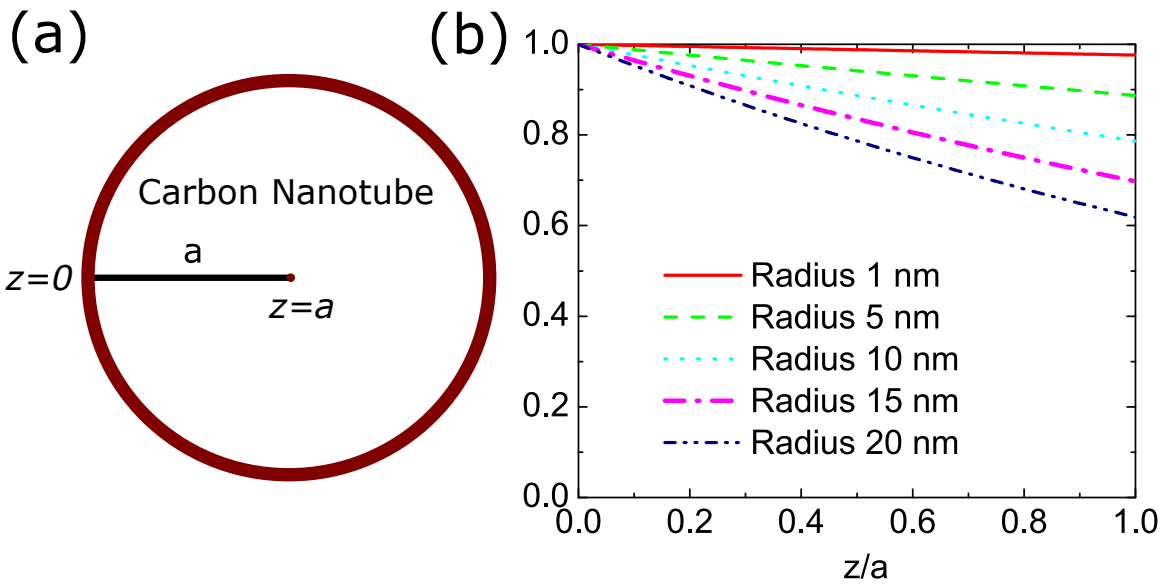

Figure 4.2: (a) The position of $z = 0$ and $z = a$ in the model, measured from the interface between CNT and cancer cells. (b) The exponential term in the heat source. We assume the heat source is constant to simplify the problem.

the radius of CNT more than 15 nm, the decayed is less than 0.8. This assumption is still useable if the radius of CNT is less than 15 nm.

This assumption is also reasonable, since in the real case, CNT is not rigid tube, there is empty space on the inner side of the nanotube. By neglecting exponential term, the calculated temperature profile on the inner side of the nanotube might be slightly higher than its expected temperature. The simplified heat source is defined as,

$$q = (1 - R)I_0 \, \alpha. \tag{4.10}$$

4.3 Solution of model

Equation (4.3) should be integrated in order to solve the heat equation. The results of integration can be written as,

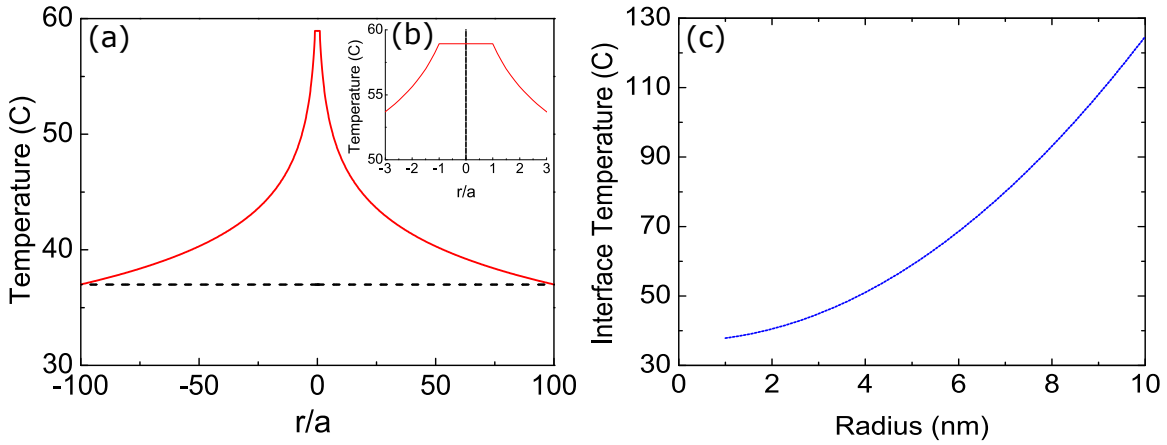

Figure 4.3: (a) The temperature of CNT and its surrounding during laser heating process. The radius of CNT in this ploot is 5 nm. (b) The temperature profile inside the CNT, region of $0 < r < a$, the temperature slightly constant from the center to the radius. However, the maximum temperature is located at the center of the tube. (c) The Interface temperature during laser heating as a function of CNT radius. The physical parameters can be seen in Table 4.1.

$$\frac{dT}{dr} = -\frac{qr}{2k_c} + \frac{ck_1}{r}, \tag{4.11}$$

where ck_1 is constant and its value should be zero, in order to satisfy the boundary conditions in equation (4.5). Consequently, the equation become,

$$\frac{dT}{dr} = -\frac{qr}{2k_c}. \tag{4.12}$$

The general solution at $0 < r < a$ can be obtained, by integrating equation(4.12). The general solution is given by

$$T(r) = -\frac{qr^2}{4k_c} + ck_2, \tag{4.13}$$

where ck_2 is constant.

The solution of the heat equation at $r > a$ region can be obtained by integrating equation(4.4). The result of integration can be defined as

$$\left(\frac{dT}{dr}\right) = \frac{ct_1}{r}, \tag{4.14}$$

where ct_1 is constant. By integrating equation(4.14), we obtain

$$T(r) = ct_1 \ln r + ct_2, \tag{4.15}$$

where ct_2 is constant. By satisfying equation(4.6) in boundary condition, the ct_1 can be obtained. ct_1 can be defined as,

$$\begin{aligned} k_c\left(\frac{dT}{dr}\right) &= k_t\left(\frac{dT}{dr}\right) \quad \text{at } r = a, \\ \frac{-qr}{2}\bigg|_{r=a} &= k_t \frac{ct_1}{r}\bigg|_{r=a} \\ \frac{-qa}{2} &= k_t \frac{ct_1}{a} \\ ct_1 &= -\frac{qa^2}{2k_t}. \end{aligned} \tag{4.16}$$

By substituting equation(4.16) into equation(4.15), the general solution become,

$$T(r) = -\frac{qa^2}{2k_t} \ln r + ct_2. \tag{4.17}$$

Constant ct_2 can be obtained by substituting equation(4.8) in boundary conditions into general solution in equation(4.17), and defined as

$$\begin{aligned} T_b &= -\frac{qa^2}{2k_t} \ln b + ct_2 \\ ct_2 &= T_b + \frac{qa^2}{2k_t} \ln b \end{aligned} \tag{4.18}$$

By Substituting equation(4.18) into equation(4.17), the real solution for $r > a$

region can be obtained. The solution is

$$\begin{aligned} T(r) &= -\frac{qa^2}{2k_t}\ln r + \frac{qa^2}{2k_t}\ln b + T_b \\ &= \frac{qa^2}{2k_t}\ln\left(\frac{b}{r}\right) + T_b \end{aligned} \tag{4.19}$$

By considering the continuity in boundary conditions equation(4.7), the ck_2 can be defined as,

$$\begin{aligned} T(a_-) &= T(a_+) \\ \frac{qa^2}{2k_t}\ln\left(\frac{b}{a}\right) + T_b &= -\frac{qa^2}{4k_c} + ck_2 \\ ck_2 &= \frac{qa^2}{2}\left(\frac{1}{k_t}\ln(b/a) + \frac{1}{2k_c}\right) \end{aligned} \tag{4.20}$$

By substituting equation(4.20) into equation(4.13), we can obtain the real solution for the $0 < r < a$ region. The solution is

$$\begin{aligned} T(r) &= -\frac{qr^2}{4k_c} + \frac{qa^2}{2k_t}\ln\left(\frac{b}{a}\right) + T_b + \frac{qa^2}{4k_c} \\ &= \frac{q}{4k_c}\left(a^2 - r^2\right) + \frac{qa^2}{2kt}\ln\left(\frac{b}{a}\right) + T_b \end{aligned} \tag{4.21}$$

4.4 Results

According to the solution of model, the temperature of CNT during laser heating are,

$$T(r) = \begin{cases} \frac{q}{4k_c}\left(a^2 - r^2\right) + \frac{qa^2}{2k_t}\ln\left(\frac{b}{a}\right) + T_b & \text{for } 0 \le r \le a, \\ \frac{qa^2}{2k_t}\ln\left(\frac{b}{r}\right) + T_b & \text{for } r > a. \end{cases} \tag{4.22}$$

Based on the equation (4.22), the maximum temperature during laser irradiation is located at the center of cylinder. Then, the temperature decreases from center to the interface of CNT and cancer cells. However, the results are obtained by assuming the heating function is constant as shown in equation (4.10). Consequently, the calculated temperature at the center of CNT is slightly higher than its reality.

Table 4.1: The physical parameters of laser, cancer cells and CNTs.

Physical parameters		
Thermal conductivity of human tissue	k_t	0.567 W/mK [94]
Thermal conductivity of CNTs	k_c	3000−3500 W/mK [25]
Initial temperature	T_∞	37^o C
Reflectivity	R	0.1
Absorption coefficient of CNTs	α	2.4×10^7 m^{-1} [95]
Laser intensity	I_0	1×10^6 W/cm^2 [96]
Radius of SWNT	a	5 nm
The farthest considered distance	b	100 a

The temperature during the laser irradiation is proportional to the radius of cylinder (a) as shown in equation (4.22). Thus, we suggest to use the larger diameter of CNT to maximize the laser heating process. We plot the temperature profile during laser heating process as shown in Figure 4.3(a)and(b). We select the radius of CNT is 5 nm. The physical parameters can be seen in Table 4.1.

The temperature at the interface between CNT and cancer cells can be written as,

$$T(a) = \frac{qa^2}{2k_t} \ln\left(\frac{b}{a}\right) + T_b. \tag{4.23}$$

Based on equation(4.23) and equation(4.22), we found that the interface temperature is proportional to the square of CNT radius. Consequently, we suggest using the longer diameter of CNTs in order to get the maximum temperature during therapy.

4.5 Conclusions of laser heating carbon nanotubes

We have developed the theoretical model of laser heating CNTs by assuming the CNT as a solid cylinder. The temperature profile in CNT and its surrounding during laser heating process is determined by solving classical heat conduction equation. According to our calculation results, the maximum temperature during laser heating process is located at the center of CNT because we neglect the exponential term

of heating function. Correspondingly, the calculated temperature inside the CNT is higher than its fact.

The temperature during laser heating process is proportional to the radius of CNT. The suggested specification of CNTs for theranostic agents is the CNTs with larger diameter to maximize the laser heating process.

Chapter 5

Carbon nanotubes as theranostics agents

In this chapter, the usage of CNT as contrast agents of PA imaging and heating agents of PTT will be explained. The effect of laser to the CNT will be discussed based on the experimental results. Some materials in this chapter were published in the proceeding of meetings on acoustics with title "Carbon nanotubes as potential candidate for photoacoustic imaging"[20] and also in in the Nanomaterials with title "A Theoretical Model of Laser Heating Carbon Nanotubes"[88].

5.1 Introduction to contrast agents and heating agents

PA signal is produced based on the ability of the object to absorb the light. The hemoglobin is a good chromophore for the green light as explained in the chapter 2. However, not all of the target is a good chromopore of green light. For example, breast tumor. Breast tumor is good infrared absorber as shown in Figure 5.1. The breast tumor strongly absorbs the light in the range of 900-1000 nm[97]. By injecting contrast agents to the target, we can obtain the PA image of tumor using green laser. We can also enhance the contrast between the center of interest and the background.

The advantage of using contrast agent is the possibility to combine the diagnostic

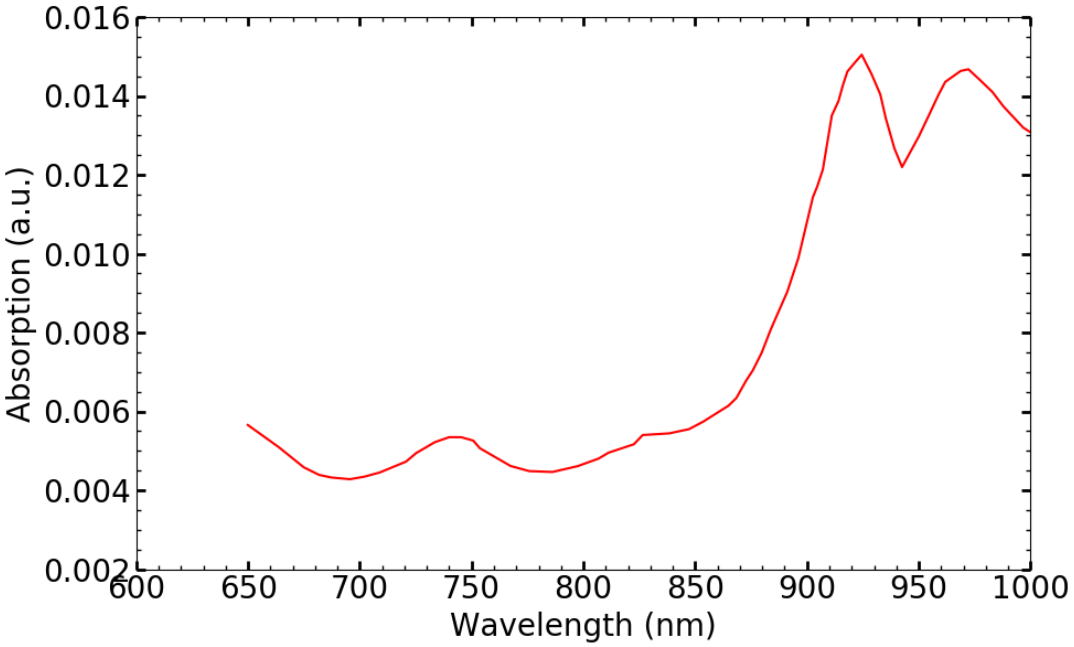

Figure 5.1: Optical absorption spectra of malignant breast tumors. Data were taken from Cerussiz Albert *et al.* [97].

and therapy at the same time, which is called theranostics[98, 99, 100]. Consequently, the contrast agents of PA imaging and the heating agents of PTT are called theranostics agents[101].

The potential candidate materials for theranostics agents should have strong optical absorptions and broad in the visible as well as infrared regions. CNTs have very strong and broad optical absorption in the visible and infrared regions. Correspondingly, we propose to use CNTs as potential candidate materials for theranostics agents.

5.2 Absorption spectra of carbon nanotubes

We use SWNT(6,5) as our CNT sample as explained in the Section 3.5. The optical absorption spectra of CNT is measured by using UV-Vis spectrometer and A-mode

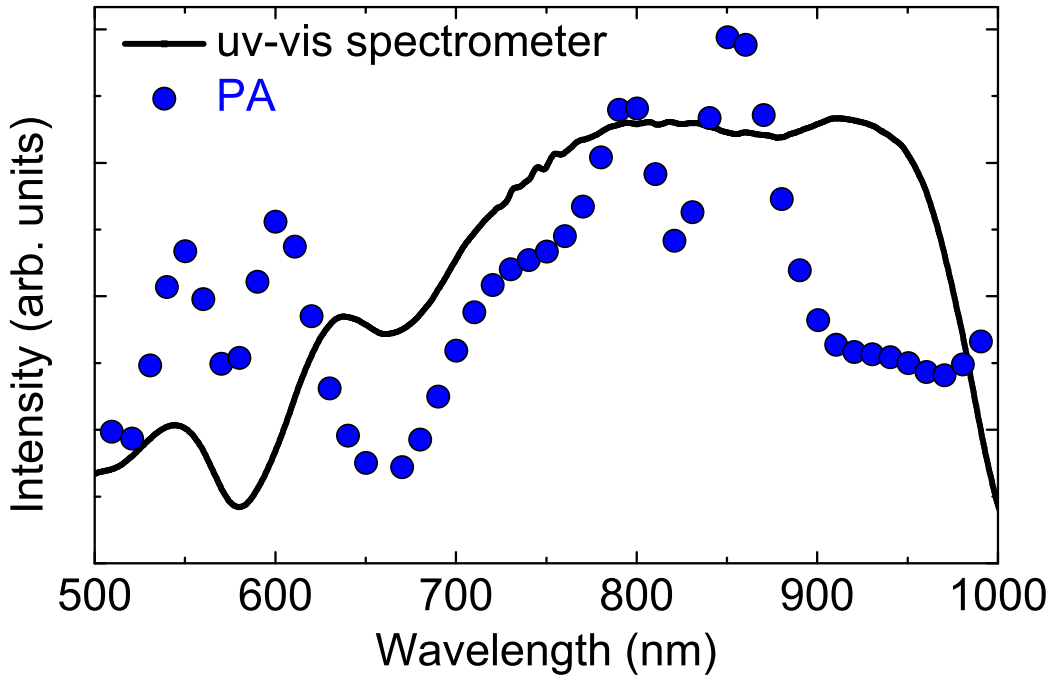

Figure 5.2: Optical absorption spectra of CNT measured by using UV-VIS spectrometer and PA imaging with tunable laser.

PA imaging with tunable wavelength laser. The results of absorption spectra measurements can be seen in Figure5.2.

Both measurement results confirm that CNT has strong and broad optical absorption. Visually, two peaks exist in the optical absorption spectra of CNT. The first peak is located in the 800 nm - 840 nm (infrared regions) while the second peak is located in the 500 nm - 580 nm (visible regions). The broad optical spectra of CNT is reasonable since the color of our sample is black which means CNT absorbs all of visible light. However, both measurements confirmed that the first peak is stronger than the second peak. According to the experimental result from *Robinson et al.* that we mentioned in Chapter 1, the absorption spectra of CNT is high in all visible-infrared region in compared to gold nanorod[11]. Although 532 nm is not the strongest peak, we will use 532 nm laser in this research.

The optical absorption spectra proved that CNT is a potential candidate for con-

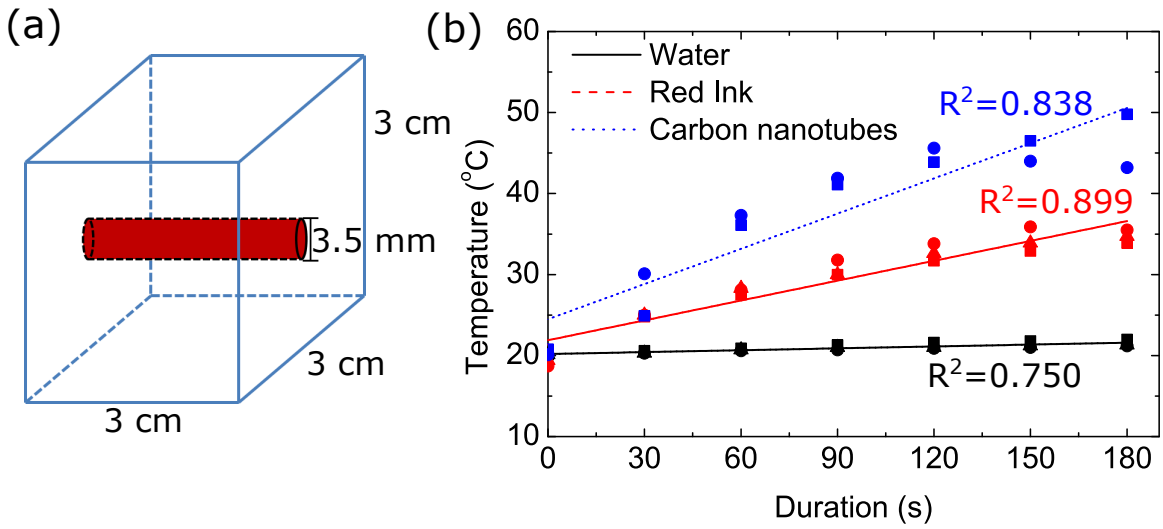

Figure 5.3: (a) The schematic diagram of the phantom, and (b) the temperature as a function of the laser heating duration for several samples, water, red ink and CNT.

trast agent in PA imaging, especially with the infrared laser. The infrared region has an advantage in PA imaging since the PA signal from deep tissue can be obtained.

5.3 Laser Heating Experiments

The PA signal is generated as a consequence of the rise in temperature of the object. Hence, the temperature of the object is increased by laser irradiation, thus the PA signal is created. In this section, we want to evaluate the PA properties of CNT by evaluating the gradient of temperature during laser irradiation.

We created a ultrasound phantom in order to describe the real situation of laser heating process in the tissue. The ultrasound phantom is made by Polyvinyl alcohol(PVA) as basic material and dimethyl sulfoxide (DMSO) as solvent. The size of phantom is cube with size 3 cm $\times$ 3 cm $\times$ 3 cm. We made a hole from left side to the right side of cube in order to inject the samples. The schematic diagram can be seen in Figure 5.3(a).

The specification of laser are PRF 10 kHz, wavelength 532 nm, pulse duration 5.9

ns and power ± 30 A (2.5 Watt). We measured the temperature of the samples every 30 second in 3 minutes. We prepared three samples; water, red ink, and CNT. Red ink is used to represent the blood since the red ink and blood have similar optical absorption. The experiments were performed at the room temperature 20°C.

The experimental results of laser heating CNT can be seen in Figure5.3(b). The CNT data have the highest temperature in compared to water and red ink. The slope of CNT data is 0.14 °C/s which means the temperature is increased 0.14 °C every second. The slope of the red ink 0.081 °C/s and the slope of water 0.007 °C/s.

The rise in temperature of the CNT is enough to kill the cancer cells in the PTT. The rise in temperature causes the cancer cells to become hyperthermic and damaged. The cancer cells become damaged due to the destitute of blood supply caused by the temperature reaches to the 41-47 °C for several time [91, 90].

5.4 PA Signal of CNT

We scanned the CNT and red ink with several percentages of concentration under the OR-PAM system with 532 nm laser. We injected the solution of CNT into the micropipe. We made several different samples for comparison. First, the pure solution of CNT. The second, pure red ink. Third, a mixed solution of 95 % CNT and 5% red ink. The fourth, a mixed solution of 50 % CNT and 50% red ink. The definition of the percentage in this work is percentage of volume. The samples were injected into the micropipe with the same diameter as can be seen in Figure5.4(a).

We compared the four samples as shown in Figure 5.4(b). The raw images were bandpass filtered along the center frequency of the transducer. Then, the images were projected by using MIP. The 100 % red ink is the lowest intensity. By adding 5% of CNT, the intensity was enhanced. However, the highest intensity is not the solution of 100 % CNT but the solution of 50 % CNT and 50% red ink. The possible

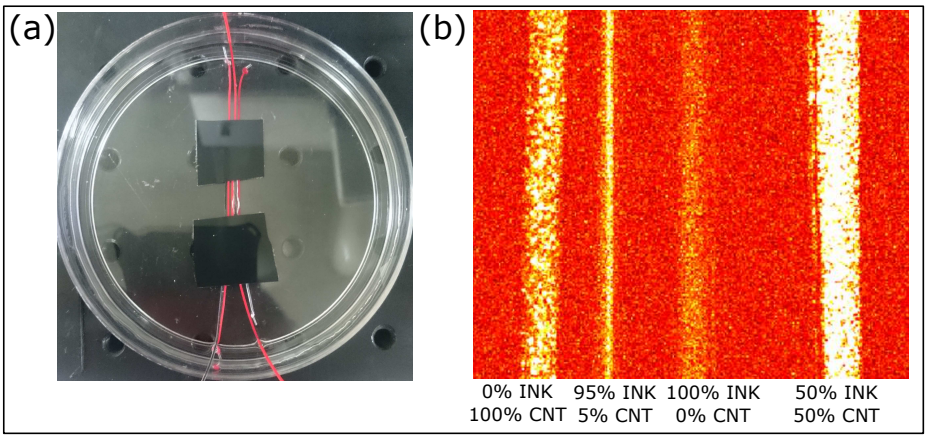

Figure 5.4: (a) The photograph of samples (b) the sample under the PAM.

reason is the the solution of 50% CNT and 50 % red ink changes the color of solution to become dark red. The solution of dark red strongly absorbs the green light. The bright points in the image is the powder of CNT which still does not dissolve in the solution.

5.5 Summary of CNT as heating theranostics agents

We have shown the measurement results of optical absorption spectra of CNT. The optical absorption spectra of CNT is high and broad in the visible and infrared regions. The result is consistent with the previous work [11]. The laser heating experiment confirm that the CNT has highest gradient of temperature during laser irradiation. The gradient of CNT is 0.14 °C/s which means the temperature is increased 0.14 °C every second.

The PA image of several samples conclude that by adding CNT to the red ink, the PA signal will be significantly enhanced. The highest intensity is solution of 50 % CNT and 50% red ink. The experimental results confirm the ability of CNTs as theranostics agents.

Chapter 6

Photoacoustic image denoising using non-local means denoising

In this chapter, the PA image denoising using Non-local means denoising (NLMD) method will be discussed. The suggested input parameters to apply NLMD method in PA imaging are also discussed. Some materials in this chapter are published in the Japanese Journal of Applied Physics, with title "Non local means denoising in photoacoustic imaging"[102].

6.1 Introduction to NLMD

PA image is normally degraded due to noise. Several source of noise are the time delay error of PA wave by choosing inappropriate speed of sound[103], transducer dimension[6, 104, 105], and laser-induced component[106].

We would like to remove the noise from PA image by using NLMD method[107, 108, 109]. We choose NLMD method because it has successfully applied in the another biomedical imaging such as magnetic resonance imaging (MRI)[110, 111, 112], ultrasound imaging[113, 114], positron emission tomography (PET)[115, 116] , and computed tomography (CT)[117, 118]. Previous works mentioned that the NLMD can be used to increase PSNR image without destroying noticeable image structure[110]. NLMD also effectively smoothing the homogenous area in the image[111].

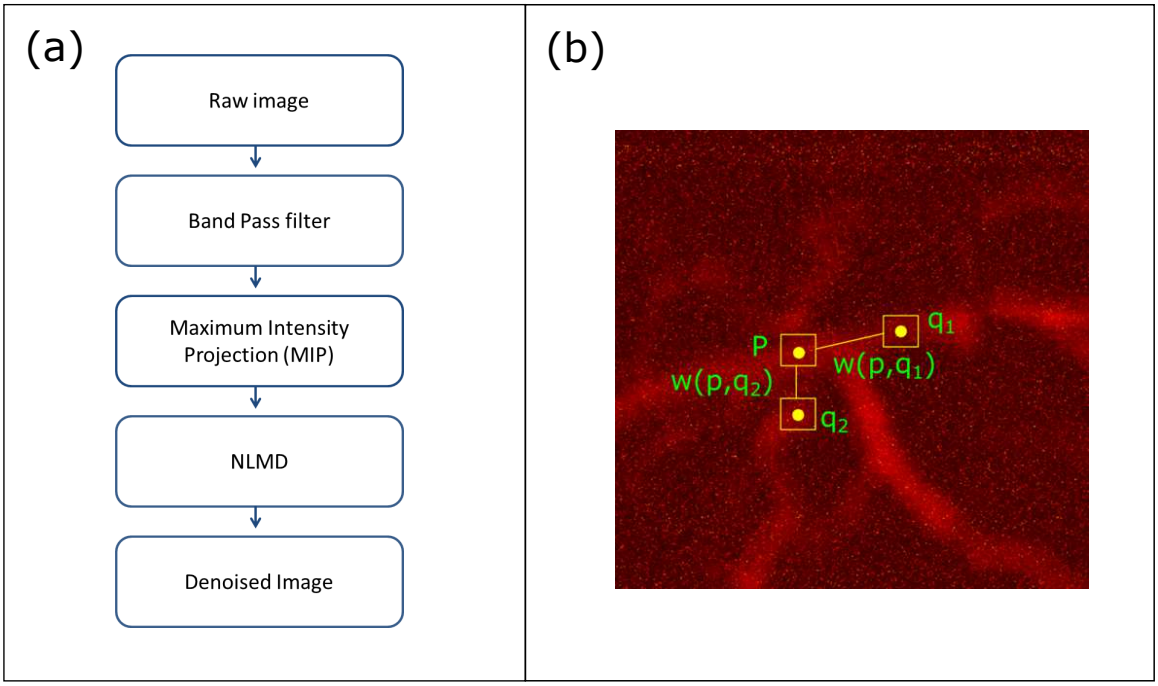

Figure 6.1: (a) The algorithm of proposed denoising method using NLMD (b) Example of self-similarity in the PA image. The image is the mice brain. p,q_1 and q_2 are similar.

The NLMD can be applied to the image if self-similarity exist in the image. In Figure6.1(b), we show the example of self similarity. Basically, similar patch contain noise and true image,

$$I_i = T + N_i \tag{6.1}$$

where I_i,T,N_i, and i respectively are image in the patch, true image, noise and index of patch. Because noise is random, so if we take average average of all the similar patch, the noise will be suppressed. Therefore, the idea of NLMD is replacing all of the pixels in the image by computing the weighted average of nearby similar patch[107, 108]. The appropriate input parameters to apply NLMD method to the PA image will also be discussed. The appropriate input parameters will be evaluated from several experiments.

6.2 Peak signal-to-noise ratio

Peak signal-to-noise ratio (PSNR) is important parameter in the image denoising. The definition of PSNR is the ratio between maximum peak of power signal and the maximum peak of power noise. The quality of image can be evaluated by measuring the PSNR. The PSNR of grayscale image is given by

$$\mathrm{PSNR}(f,g) = 10 \cdot \log_{10}\left(\frac{Max_I^2}{\mathrm{MSE}(f,g)}\right), \tag{6.2}$$

with

$$\mathrm{MSE}(f,g) = \frac{1}{mn}\sum_{i=0}^{m-1}\sum_{j=0}^{n-1}\left(f_{i,j} - g_{i,j}\right)^2. \tag{6.3}$$

where f is the true image and g is noisy or denoised image. i, j denotes the pixel positions. MSE is the abbreviation for mean squared error. The unit of PSNR is decibel (dB).

6.3 Bandpass filter

The PA signal in PA imaging is detected by using ultrasound transducer as explained in Section 2.3. The bandpass filter remove the low and high frequency components. In this preprocessing method, the used frequencies are low frequency 5 MHz and high frequency 100 MHz. We selected the low and high frequencies based on the center frequency of transducer, which is 50 MHz.

In Figure 6.2, we show the frequency response of bandpass filter. We used order = 2 in our research.

We apply the bandpass filter to the acquired 3D data. The A line profile of raw data and a bandpass filtered data can be seen in Figure 6.3. After applying the bandpass filter to the A-line data, the ripple in the peaks disappeared. The 2D of PA image is reconstructed by joining the maximum intensity of each A-line.

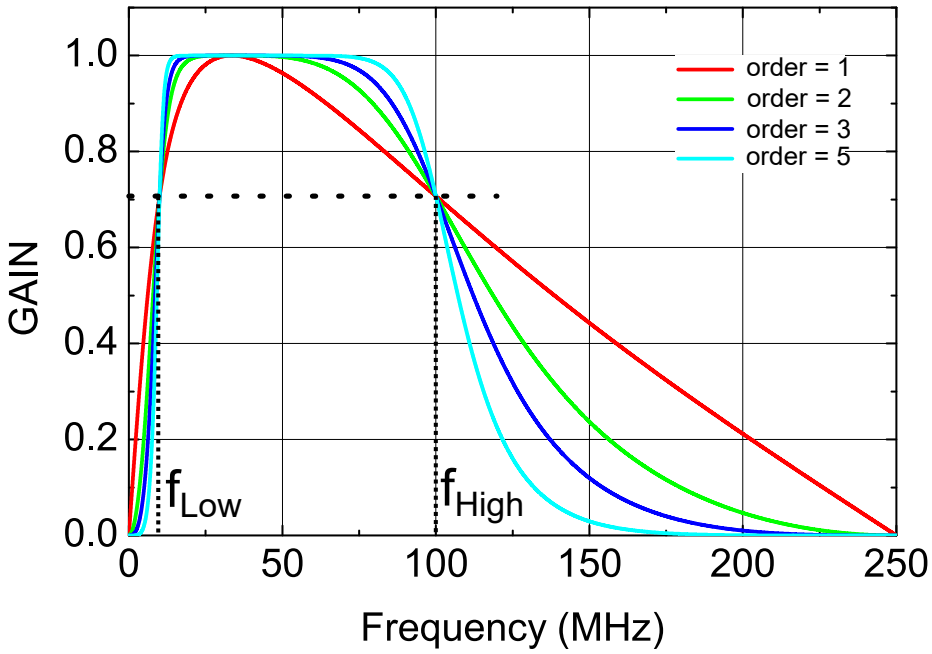

Figure 6.2: frequency response of bandpass filter

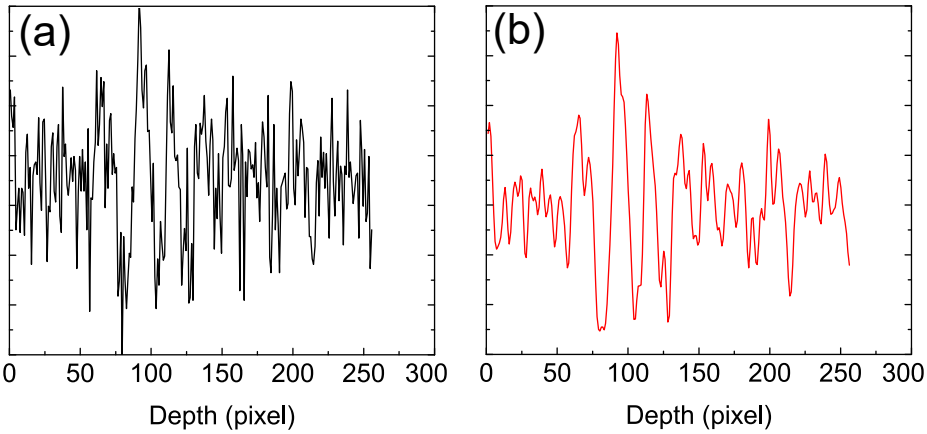

Figure 6.3: The A-line profile of PA image. (a) The raw signal and (b) bandpass filtered signal.

6.4 Algorithm of NLMD

The NLMD method has several step as shown in Figure6.1(a). The first step, the raw image is filtered by using band-pass filter around the center frequency of transducer as we explained in Section 6.3. The second, the image is projected by using the maximum intensity projection (MIP) to obtain two dimension image. In the present work, we use C mode projection as explained in Section 2.4.1. Then, we apply the NLMD method. The Equations in this section are taken from Refs.[107, 108].

The repaired pixel intensity of grayscale image ($\hat{u}$) with pixel position p according to NLMD method can be expressed as,

$$\hat{u}(p) = \frac{1}{C(p)} \sum_{q \in B(p,r)} u(q) w(p,q), \tag{6.4}$$

where u is pixel intensity of similar patch in the surrounding repaired patch, q is pixel position of the similar patch in the searching area, w is weighting factor, $B(p,r)$ is the maximum searching area, and r is the maximum distance, which is input parameter. C is the normalization factor and given by

$$C(p) = \sum_{q \in B(p,r)} w(p,q). \tag{6.5}$$

Weighting factor can be calculated by using exponential function. The weighting factor can be written as

$$w(p,q) = \exp\left(\frac{-\max(d^2 - 2\sigma^2, 0.0)}{h^2}\right), \tag{6.6}$$

where σ^2, d, and h respectively are variance of raw image, euclidean distance between two pixels, and exponential decay. Euclidean distance can be formulated as

$$d^2\left(B(p,f), B(q,f)\right) = \frac{1}{(2f+1)^2} \sum_{j \in B(0,f)} \left(u(p+j) - u(q+j)\right)^2, \tag{6.7}$$

where $B(p, f)$ is the patch of original image, which represented as P in Figure6.1(b) while $B(q, f)$ is the patch of similar image in searching area, which represented as q_1 and q_2 in Figure6.1(b). f is the size of patch, which is input parameter. j denotes the point inside the patches.

There are three input parameters exist in the NLMD method; size of patch(f), maximum distance for searching similarity (r), and exponential decay (h).

6.5 Experimental results

6.5.1 Experimental subjects

Experimental subjects were used to test the NLMD algorithm. The algorithm is tested on the three subjects.

- carbon nanotube filled micropipe.
- *in vivo* mice ear vessels.
- *in vivo* mice brain vessels.

6.5.2 Calculation tools and software

We used Python 3.6, NumPy[119], scikit-learn[120] and scikit-image[121] to implement the algorithm. The images were plotted by using matplotlib in python[122].

6.5.3 Carbon nanotube filled micropipe

We use carbon nanotube filled micropipe in order to obtain the synthetic data of free noise image. The process to obtain synthetic data can be seen in Figure6.4. First, the raw image is filtered by using the bandpass filter. The showed raw image in Figure6.4 is the 2D projection of 3D raw data. The definition of bandpass filtered image is also 2D projection of 3D bandpass filtered data. A single depth (A-line) data before and after applying bandpass filter can be seen in Figure 6.3. The bandpass filtered image

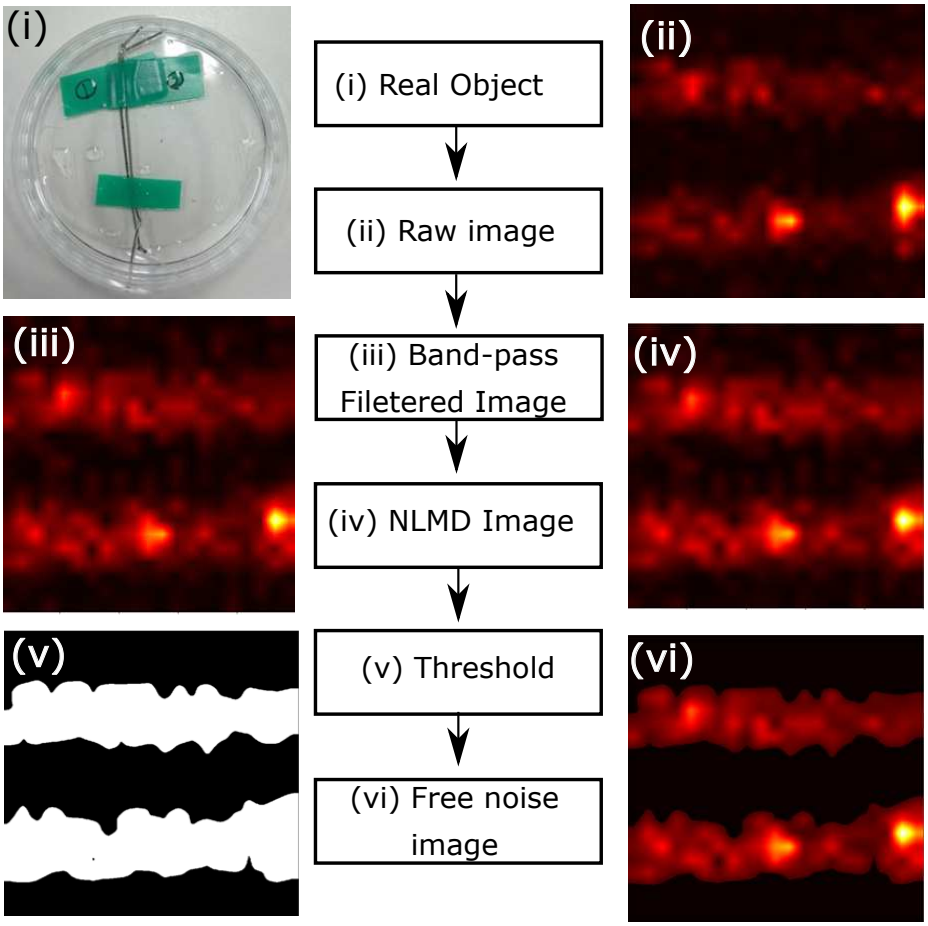

Figure 6.4: Schematic process to extract free noise image from CNT filled micropipe. (i) The real object, (ii) 2D (MIP) projection of raw data, (iii) 2D (MIP) projection of 3D band-pass data, (iv) NLMD image, (v) thresholded image, and (vi) free noise image.

is filtered by applying NLMD method. We threshold the NLMD image by using Otsu method[123]. Finally, the NLMD image is masked with threshold image in order to obtain the free noise image.

The free noise image is used to investigate the effect of noise to image. Then, the noisy images is used to investigate the reparation of image after applying NLMD to the noisy image. So, easily we can calculate the PSNR of image as explained in Section 6.2.

6.5.3.1 Noisy images

We add several percentages of random noise from 7 % to 100 % into the free noise image. The percentage of noise is measured relative to the variance (σ^2) of free noise image. The equation of adding noise into free noise image is given by

$$NI = FNI + \sigma^2(FNI) \times \text{rand}(), \tag{6.8}$$

where NI,FNI, and rand() respectively are noisy image, free noise image, and random number. Then, NI is normalized so the maximum pixel intensity is one.

In Figure6.5(a), we show several results of the noisy images. We can see that by increasing the percentage of noise, the quality of image becomes decreased. This statement also confirmed by the PSNR of noisy image. The PSNR of noisy images be seen in Figure6.6(a). The PSNR is calculated by using equation(6.2).

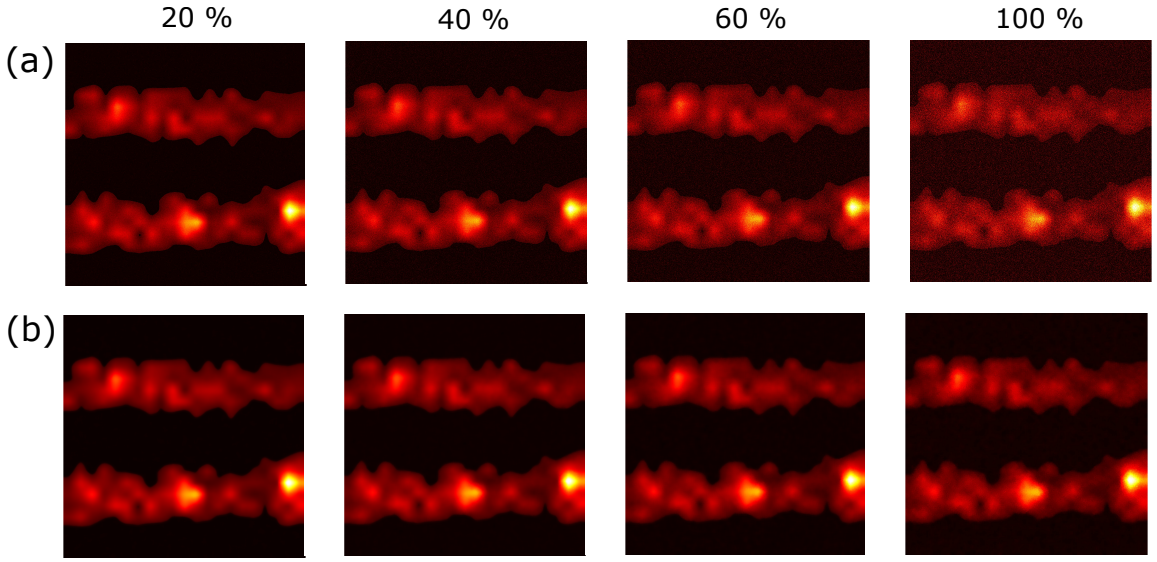

Figure 6.5: Images of carbon nanotube filled micropipe (a) Noisy images. By increasing the percentage of noise, the image become more corrupt. (b) The denoised images.

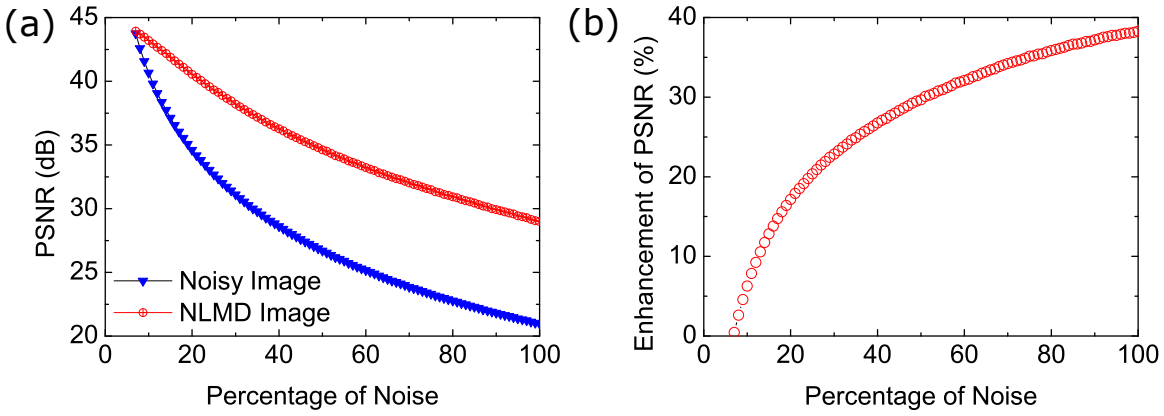

Figure 6.6: (a) The PSNR as a function of percentage of noise for noisy and NLMD images. The PSNR is calculated relative to the free noise image as shown in in Figure6.4. (b) The percentage of PSNR enhancement as a function of percentage of noise.

6.5.3.2 Denoised images

The noisy images were denoised by using NLMD method. Several results can be seen in Figure6.5(b). We can see that the images are well repaired after applying NLMD method. According to the PSNR, the PSNR of denoised images is always higher than the PSNR of noisy images, as shown in Figure6.6(a). Therefore, the NLMD method can be used for highly degraded image. The maximum enhancement of PSNR in the denoised image of carbon nanotube filled micropipe is 38%. The input parameters will be discussed at the next subsection in this chapter.

6.5.3.3 Input parameters

To automatically apply NLMD method, the suitable input parameters should be defined. The input parameters exist in the NLMD method are size of patch (f), maximum distance for searching similarity (r) and exponential decay (h). The suitable parameters are defined by several experiments of free noise image of micropipe filled carbon nanotubes. First, we add 40 % noise to the free noise image, then combine the input parameters.

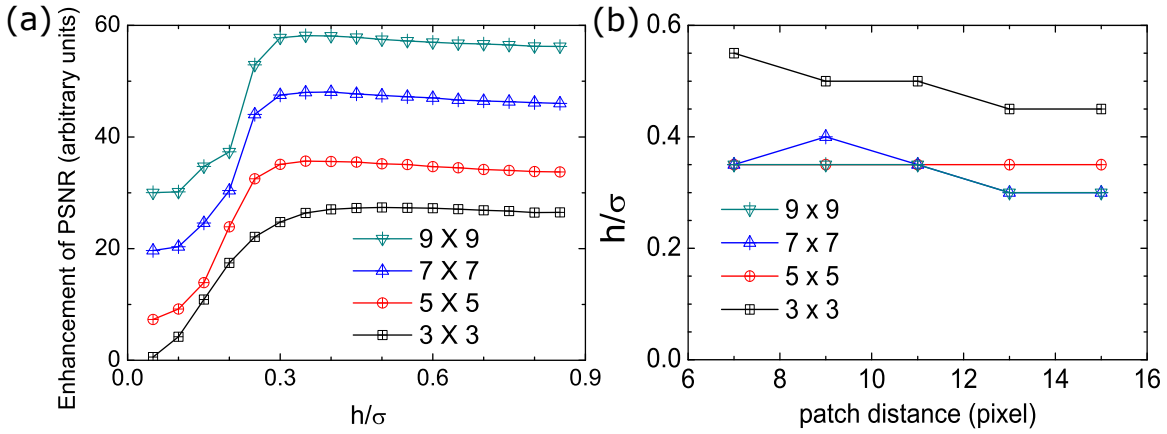

Figure 6.7: (a) The enhancement of PSNR as a function of exponential decay. The maximum searching distance is 9. The peak positions are located in the $0.35\sigma < h < 0.55\sigma$ regions. (b) The exponential decay when the PSNR is maximum as a function of maximum patch distance.

The patches size (f) are $3\times$, 5×5, 7×7, and 9×9. Larger than these values the image becomes blurry. The suggested values of exponential decay according to the previous work[107] are $0.3\sigma < h < 0.40\sigma$. The patch distances are $7, 9, 11, 13$ and 15.

Table 6.1: The suitable input parameters of NLMD for PA image

patch size (f)	**exponential decay** (h)		
	$\boldsymbol{r}$ = 7-9	$\boldsymbol{r}$ = 10-12	$\boldsymbol{r}$ = 13-15
3×3	0.55σ	0.50σ	0.45σ
5×5	0.35σ	0.35σ	0.35σ
7×7	0.35σ	0.35σ	0.30σ
9×9	0.35σ	0.35σ	0.30σ

In Figure6.7(a), we show the enhancement of PSNR as a function of exponential decay. The peak positions are located in the $0.3\sigma < h < 0.55\sigma$ regions. We collected the peak positions(h,PSNR) then we plotted the exponential decay (h) as a function of the patch distance (maximum searching distance). The summary of the suggested input parameters based on our experiments can be seen in Tab.6.1. The best input parameters are pach size (f) 7×7, maximum searching distance r 9 and the exponential decay (h) 0.35σ, with σ denotes the standard deviation. We use these input

parameters for all of experiments in this research.

6.5.4 *In vivo* experiments

We applied the NLMD method to the real PA images. The size of acquired raw data is $256 \times 400 \times 400$. The spatial resolution is 400×400 with each point has 256 depth profile.

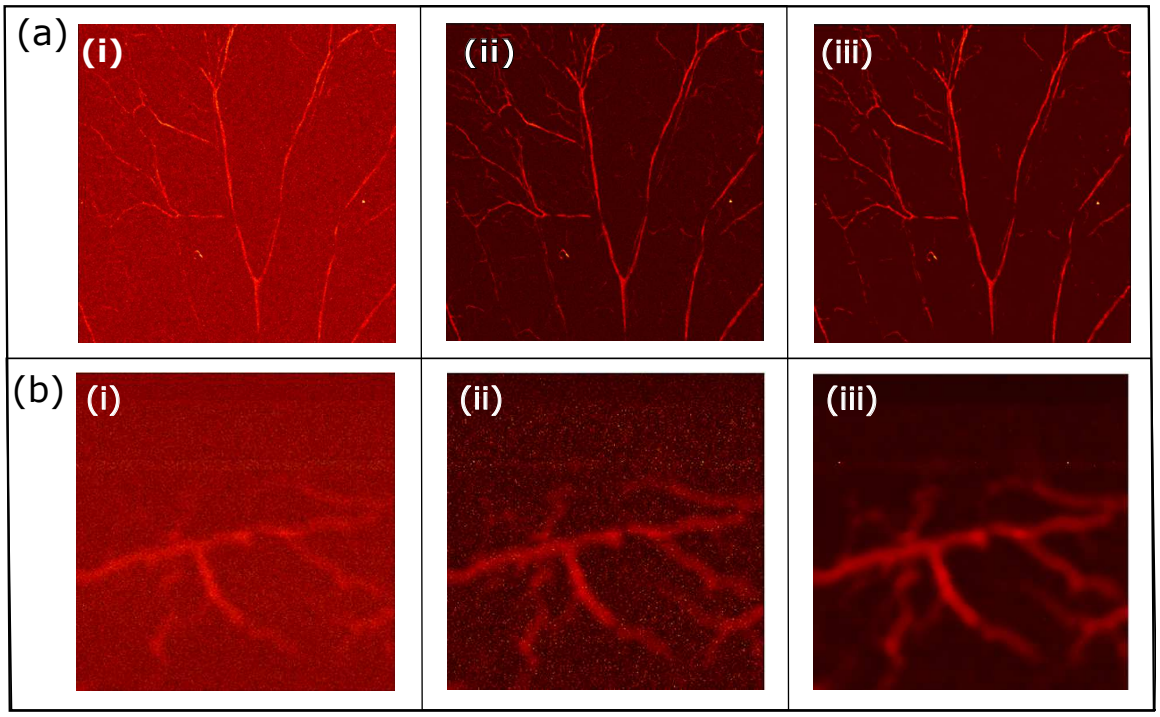

Figure 6.8: (a) *in vivo* mice ear images (b) *in vivo* mice brain images. (i) Raw images (ii) band pass filtered images and (iii) NLMD images. The images are MIP of C mode.

In Figure6.8, we show the results of *in vivo* ear and brain vessels. The raw images are contaminated by noise. Visually, the contrast of the vessels and the background are low. By applying band-pass filter the noise are suppressed and the contrast become better. We applied NLMD method to the band-pass filtered images. The contrasts of NLMD images are better than band-pass filtered images. The noise level also suppressed and the images become smooth.

6.6 Summary of NLMD method

We have successfully applied NLMD method to the PA images. The NLMD method enhances the PSNR up to 37 %. The contrast of the images is also enhanced after applying NLMD method. The suggested input parameters are patch size (f) 7×7, maximum searching distance r 9 and the exponential decay (h) 0.35σ, with σ denotes the standard deviation.

Chapter 7

Photoacoustic image denoising using dictionary learning

In this chapter, the PA image denoising using sparse code dictionary learning method are discussed. Some Materials in this chapter were presented in the 3rd International Conference on Biomedical Signal and Image Processing and will be published on international conference proceeding by ACM.

7.1 Introduction to dictionary learning

Sparse representation is modeling data vectors as sparse linear combination of basis elements. Sparse representation is recently used in the signal processing, statistics and machine learning[124]. Online Dictionary learning or sparse dictionary learning is process to find over-complete based on linear combination of an overcomplete set of signal or atoms[125].

Denoising image using dictionary learning was already successfully implemented on the MR image[126, 127, 128], CT (computed tomography) image[129, 130, 131] and ultrasound[132]. These previous work motivated us to apply dictionary learning to the PA image.

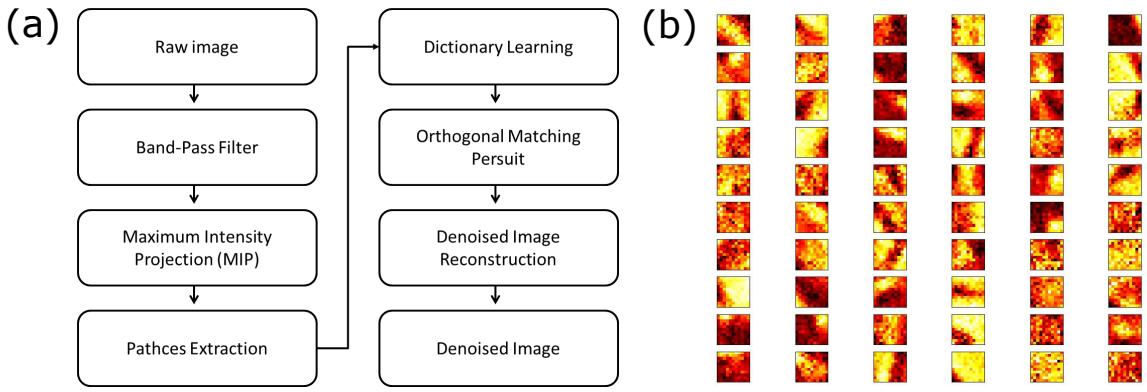

Figure 7.1: (a) The flow chart of the proposed denoising image (b) The example of dictionary.

7.2 Algorithm

The measured PA image can be modeled as

$$y = x + u \tag{7.1}$$

where y, x and u measured PA image, the true image and noise. We would like to obtain the true image or at least similar to the true image.

The proposed denoising method has several steps as shown in Figure7.1(a). In the first step, the raw image is filtered by using bandpass filter along the center frequency of the transducer. The bandpass filter remove the low and high frequency components of the signal as explained in Section 6.3.

The 2-D image is extracted into a collection of the patches. Then, the dictionary is trained by extracted patches. We use mini-batch dictionary learning[124] which is freely available in scikit-learn in python [120].

Basically the dictionary learning is method to solve the optimization problem,

$$(U^*, V^*) = \arg\min_{U,V} \frac{1}{2}||X - UV||_2^2 + \alpha||U||_1 \tag{7.2}$$

with

$$||V_k||_2 = 1 \text{ for all } 0 \leq k < n_{\text{atoms}}, \tag{7.3}$$

where $\mathbf{V}$ is the dictionary with each column represents the basis vector and α is a regulation parameters[124, 133].

There are several input parameters in the proposed method, the dictionary size, and the patch size. Another input parameters are the number of iteration, but we tune the number iteration to be fixed 500.

7.3 Experimental results

In this section, the experimental subjects and experimental results will be explained. The input parameters will be evaluated based on experimental results.

7.3.1 Experimental subjects

In this work, we were using carbon nanotube in micropipe and *in vivo* mice ear as our experimental subjects. The CNT is used to produce the synthetic image to evaluate the input parameters. The animal experiments were approved by ethical committee review board of Tohoku University. We used Python 3.6, NumPy[119], scikit-learn[120] and scikit-image[121] to implement the algorithm. The images were plotted by using matplotlib[122].

7.3.2 Carbon nanotube filled micropipe

The carbon nanotube is used to obtain the free noise image. The enhancement of the image quality is measured relative to the free noise image. The size of raw data is 256×300×300. The 256 is the A-line, which is the data of the depth in a point. 300×300 are width and the length points of image.

There are several steps in to obtain free noise image. First, we applied a bandpass filter around the center frequency of transducer to the raw image. The second, the image is projected by using maximum amplitude projection to obtain 2D image. We applied non-local means denoising (NLMD) to the 2D image of CNT to suppress the

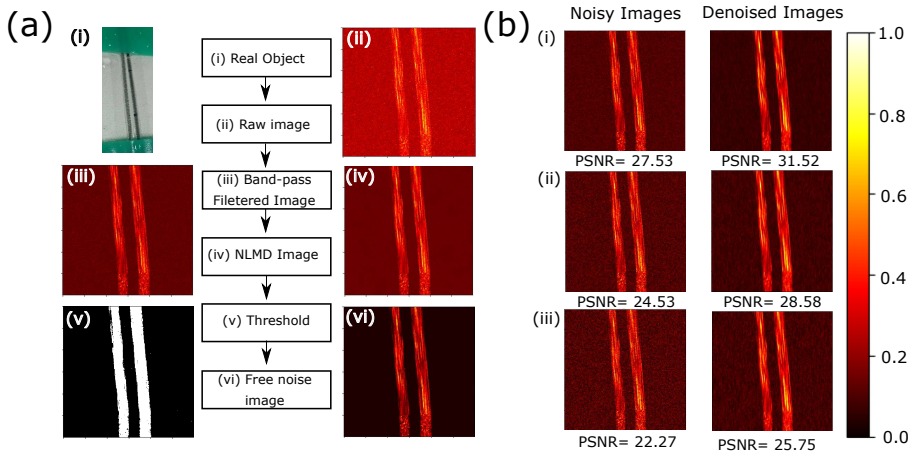

Figure 7.2: (a) Process to extract the free noise image from noisy image. (i) The real object,(ii) 2D projection of raw image, (iii) 2D projection of bandpass filtered data, (iv) NLMD image, (v) thresholded image, (vi) the free noise image. (b) Noisy and denoised images where percentage of noise (i) 40 %, (ii) 60 %, and (iii) 80 %.

noise [102]. Then, the image was thresholded by using Otsu method[123]. We masked the thresholded image with the NLMD image to obtain the free noise image. Please see Figure7.2 for more details.

We added several percentages of random noise from 25% to 100 % into the free noise image. The percentage of noise is measured relative to the variance (σ^2) of the free noise image. The several results of noisy images can be seen in Figure7.2(b). Visually, by adding the noise, the image quality become worse. The image quality also confirmed from the PSNR of noisy image. The PSNR of noisy images is decreased by increasing the percentage of noise as shown in Figure7.3(b).

We applied proposed denoised method to the noisy images of CNT. Several results can be seen in Figure7.2(b). The noise is successfully suppressed. The used input parameters were patch size 9×9 and the dictionary size 300. The PSNR of denoised images were always higher than PSNR of noisy images. These results showed that the proposed denoised method always enhance the image quality. The proposed method can be used even for high degraded image.

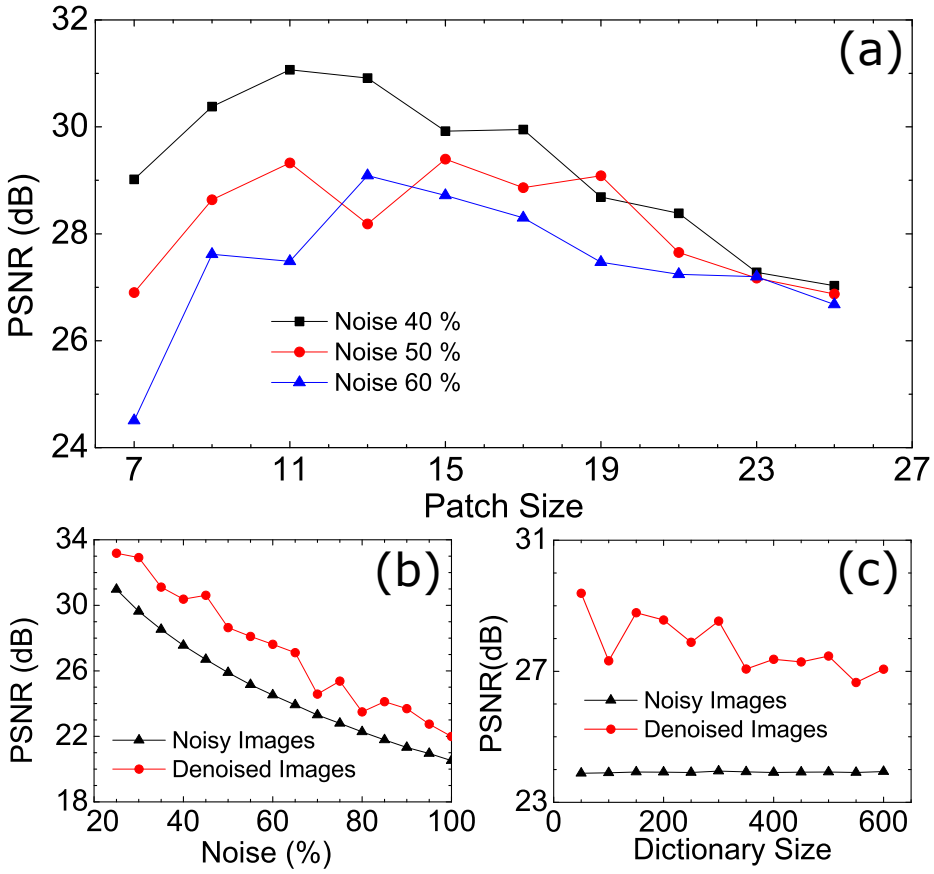

Figure 7.3: PSNR as a function of several parameters (a) patch size, (b) percentage of noise, and (c) dictionary size.

7.3.3 Input parameters

In this subsection the input parameters of proposed denoising method using dictionary learning will be discussed. The input parameters in the proposed methods were the patch size and the dictionary size. The patch size should be odd number in order to accommodate the center. The numerical parameters of iteration such as the number of iteration and the mixing parameter are assumed to be constant. Moreover, all of the calculation is assumed to be convergence. The input parameters is selected based on the experiments of CNT in micropipe.

In the Figure7.3(a), we showed the PSNR as a function of the patch size. The trend of the curve looks like parabola. The peaks position are located in the range of

11×11, 13 ×13 , and 15× 15 for all of the noise level.

We also plotted the PSNR as a function of the dictionary size as shown in Figure7.3(c). The input parameters are patch size 11×11 and the percentage of noise 65%. The data of PSNR is not stable. However, we see that the trend of the curve, the PSNR is decreased by increasing the dictionary size. The optimum dictionary size are 50 to 200.

Based on our experiments, the best input parameters to obtain highest PSNR are dictionary size 50 to 200 and the patch size 11×11, 13 ×13 , or 15× 15. The future study to select the input parameter based on statistical analysis is needed. The algorithm to learn the dictionary should be improved to reduce the computational time.

7.3.4 *In vivo* experiments

This subsection describes the results of the *in vivo* of ear mice. The acquire size of raw data is 256×400×400. The 256 represent the number of point to the depth direction, and 400×400 are width and length of the images. The images were projected by using MAP method.

Figure7.4 shows the results of *in vivo* experiments of mice ear. The top and bottom images are the same object on the different orientation and position. The raw images are contaminated by noise. The contrast between the vessels and the background of raw images is very low. Consequently, the vessels and the background is difficult to distinguish.

The raw images then filtered by using bandpass filter along the center frequency of the transducer. The bandpass filter removes the high and low frequency components in order to suppress the unwanted signal. The bandpass filtered images can be seen in Figure7.4(b). The contrast between the vessels and the background of bandpass

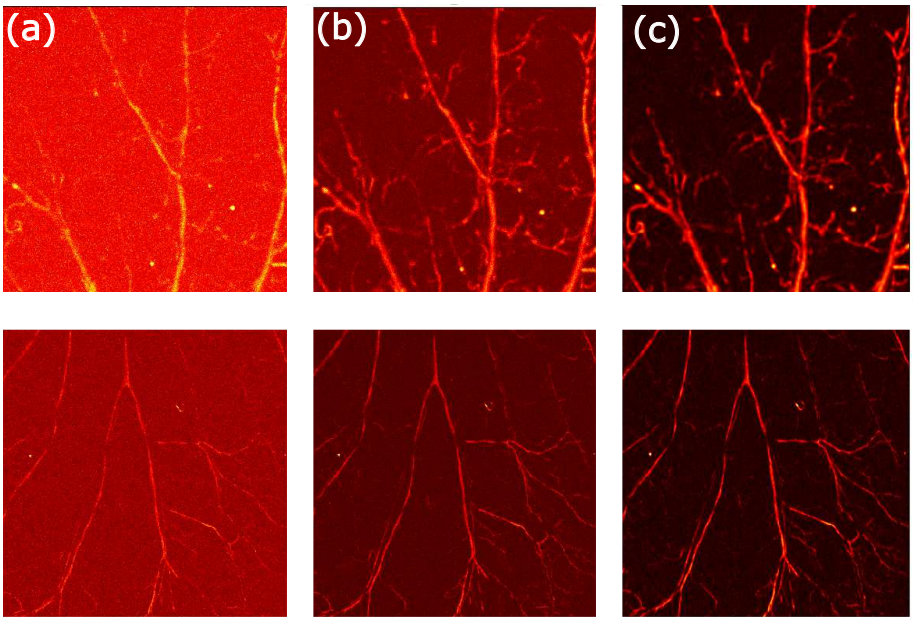

Figure 7.4: *In vivo* mice ear (a) raw images, (b) band-pass, and (c) denoised image using dictionary learning.

filtered images is better than the contrast of raw images. However, the noise still distributed in the bandpass filter images because the noise is randomly distributed in the bandwidth frequency.

The bandpass filtered images were then denoised by using proposed method, dictionary learning. The proposed method successfully removes the noise from the mice ear images. The background of the denoised images is darker than bandpass filtered or raw images. Consequently, the contrast of the denoised image is the best in compared to raw or bandpass filtered images. The proposed denoised method does not destroy the noticeable image structure.

7.4 Summary of proposed denoising method using dictionary learning

We have applied the proposed denoising method using dictionary learning to the PA image of CNT and *in vivo* mice ear. Qualitatively, we showed that the image quality

of PA image was enhanced by applying proposed denoised method without destroying image structure. The PSNR also confirm about the image quality enhancement after applying proposed method. Visually, the contrast of the vessels and the background is also improved by proposed method.

The proposed method is sensitive to the input parameters. Based on the experiments, the best input parameters to obtain highest PSNR are dictionary size 50 to 200 and the patch size 11×11, 13 ×13 , or 15× 15.

Chapter 8

Conclusions

In this dissertation, we have discussed the application of CNTs as the contrast agents of PA imaging and the heating agents of PTT. We have three main purposes of the dissertation. Correspondingly, the conclusions of this dissertation can be divided into three parts as follows.

8.1 Theoretical model of laser heating CNT

The contrast agents of PA imaging is related to the laser-material agents interaction. We have successfully developed a theoretical model of laser heating CNT by using classical heat conduction equation. The CNT in our model is modeled by a solid cylinder with the length is much greater than its diameter. Based on the solution of theoretical model in the chapter 4, we can conclude that the maximum temperature during laser irradiation is proportional to the diameter of CNT. We suggest using large diameter of CNTs for PA imaging contrast agents.

8.2 CNT as PA imaging contrast agents

We have shown that the optical absorption spectra of CNT is very strong in the visible and infrared regions. Consequently, the wavelength of laser can be varying in the visible-infrared. The created PA signal is proportional to the temperature rise

during laser irradiation. Our laser heating experiment also confirmed that the CNT has highest gradient of temperature during laser irradiation. The gradient of CNT is 0.14 °C/s which means the temperature is increased 0.14 °C every second. Our PA image of several samples conclude that Visually, by adding CNT to the red ink, the PA signal will be enhanced. The highest intensity is solution of 50 % CNT and 50% red ink.

8.3 Noise removal methods in PA imaging

In this research, we propose two noise removal methods; NLMD and dictionary learning. Both methods successfully removed the noise without destroying a noticeable image structure. The experiments confirm that both methods enhance the PSNR of the images. Both methods are sensitive to the input parameters. The error in choosing input parameters causes the image become blurry.

The suitable input parameters of the NLMD methods are patch size (f) 7×7, maximum searching distance r 9 and the exponential decay (h) 0.35σ, with σ denotes the standard deviation. In the case of dictionary learning method, the best input parameters to obtain highest PSNR are dictionary size 50 to 200 and the patch size 11×11, 13 ×13 , or 15× 15.

Appendix A

Calculation programs

There are several programs in this dissertation. All the programs are written in Python 3.6. language. All the program can be found under the following directory.
D: siregar /

For simplicity, this directory will be defined as root.

Propagating pressure

Heated slab

slab.py

Heated sphere

sphere.py

Energy dispersion of graphene

graphene_code.py

Non-local-means denoising code

auto_NLMD.py

Function

image_siregar.py, ml_imaging.py

Bibliography

[1] W. C. Röntgen, "Ueber eine neue art von strahlen," *Annalen der Physik*, vol. 300, no. 1, pp. 1–11, 1898.

[2] T. Pan, T.-Y. Lee, E. Rietzel, and G. T. Chen, "4d-ct imaging of a volume influenced by respiratory motion on multi-slice ct," *Medical physics*, vol. 31, no. 2, pp. 333–340, 2004.

[3] S. Mallidi, G. P. Luke, and S. Emelianov, "Photoacoustic imaging in cancer detection, diagnosis, and treatment guidance," *Trends in biotechnology*, vol. 29, no. 5, pp. 213–221, 2011.

[4] A. G. Bell, "On the production and reproduction of sound by light," *American Journal of Science (1880-1910)*, vol. 20, no. 118, p. 305, 1880.

[5] F. Duck, "Physical properties of tissue (academic, london)," *Google Scholar*, 1990.

[6] M. Xu and L. V. Wang, "Photoacoustic imaging in biomedicine," *Review of scientific instruments*, vol. 77, no. 4, p. 041101, 2006.

[7] S. Hu and L. V. Wang, "Photoacoustic imaging and characterization of the microvasculature," *Journal of biomedical optics*, vol. 15, no. 1, p. 011101, 2010.

[8] C. Hoelen, F. De Mul, R. Pongers, and A. Dekker, "Three-dimensional photoacoustic imaging of blood vessels in tissue," *Optics letters*, vol. 23, no. 8, pp. 648–650, 1998.

[9] A. Agarwal, S. W. Huang, M. O'Donnell, K. C. Day, M. Day, N. Kotov, and S. Ashkenazi, "Targeted gold nanorod contrast agent for prostate cancer detection by photoacoustic imaging," *Journal of Applied Physics*, vol. 102, no. 6, p. 064701, 2007.

[10] P.-C. Li, C.-W. Wei, C.-K. Liao, C.-D. Chen, K.-C. Pao, C.-R. C. Wang, Y.-N. Wu, and D.-B. Shieh, "Photoacoustic imaging of multiple targets using gold nanorods," *ieee transactions on ultrasonics, ferroelectrics, and frequency control*, vol. 54, no. 8, pp. 1642–1647, 2007.

[11] J. T. Robinson, K. Welsher, S. M. Tabakman, S. P. Sherlock, H. Wang, R. Luong, and H. Dai, "High performance in vivo near-ir (> 1 μm) imaging and photothermal cancer therapy with carbon nanotubes," *Nano research*, vol. 3, no. 11, pp. 779–793, 2010.

[12] S. Mallidi, T. Larson, J. Tam, P. P. Joshi, A. Karpiouk, K. Sokolov, and S. Emelianov, "Multiwavelength photoacoustic imaging and plasmon resonance coupling of gold nanoparticles for selective detection of cancer," *Nano letters*, vol. 9, no. 8, pp. 2825–2831, 2009.

[13] S. J. Yoon, S. Mallidi, J. M. Tam, J. O. Tam, A. Murthy, K. P. Johnston, K. V. Sokolov, and S. Y. Emelianov, "Utility of biodegradable plasmonic nanoclusters in photoacoustic imaging," *Optics letters*, vol. 35, no. 22, pp. 3751–3753, 2010.

[14] X. Yang, S. E. Skrabalak, Z.-Y. Li, Y. Xia, and L. V. Wang, "Photoacoustic tomography of a rat cerebral cortex in vivo with au nanocages as an optical contrast agent," *Nano letters*, vol. 7, no. 12, pp. 3798–3802, 2007.

[15] Y. Wang, X. Xie, X. Wang, G. Ku, K. L. Gill, D. P. O'Neal, G. Stoica, and L. V. Wang, "Photoacoustic tomography of a nanoshell contrast agent in the in vivo rat brain," *Nano Letters*, vol. 4, no. 9, pp. 1689–1692, 2004.

[16] Z. Sheng, L. Song, J. Zheng, D. Hu, M. He, M. Zheng, G. Gao, P. Gong, P. Zhang, Y. Ma, *et al.*, "Protein-assisted fabrication of nano-reduced graphene oxide for combined in vivo photoacoustic imaging and photothermal therapy," *Biomaterials*, vol. 34, no. 21, pp. 5236–5243, 2013.

[17] M. A. Patel, H. Yang, P. L. Chiu, D. D. Mastrogiovanni, C. R. Flach, K. Savaram, L. Gomez, A. Hemnarine, R. Mendelsohn, E. Garfunkel, *et al.*, "Direct production of graphene nanosheets for near infrared photoacoustic imaging," *ACS nano*, vol. 7, no. 9, pp. 8147–8157, 2013.

[18] V. Krishna, N. Stevens, B. Koopman, and B. Moudgil, "Optical heating and rapid transformation of functionalized fullerenes," *Nature Nanotechnology*, vol. 5, no. 5, p. 330, 2010.

[19] A. De La Zerda, C. Zavaleta, S. Keren, S. Vaithilingam, S. Bodapati, Z. Liu, J. Levi, B. R. Smith, T.-J. Ma, O. Oralkan, *et al.*, "Carbon nanotubes as photoacoustic molecular imaging agents in living mice," *Nature nanotechnology*, vol. 3, no. 9, p. 557, 2008.

[20] S. Siregar, R. Nagoka, K. Ishikawa, and Y. Saijo, "Carbon nanotubes as potential candidate for photoacoustic imaging contrast agent," in *Proceedings of Meetings on Acoustics 6ICU*, vol. 32, p. 020018, ASA, 2017.

[21] H. K. Moon, S. H. Lee, and H. C. Choi, "In vivo near-infrared mediated tumor destruction by photothermal effect of carbon nanotubes," *ACS nano*, vol. 3, no. 11, pp. 3707–3713, 2009.

[22] F. Zhou, D. Xing, Z. Ou, B. Wu, D. E. Resasco, and W. R. Chen, "Cancer photothermal therapy in the near-infrared region by using single-walled carbon nanotubes," *Journal of Biomedical Optics*, vol. 14, no. 2, pp. 021009–021009–7, 2009.

[23] A. M. Smith, M. C. Mancini, and S. Nie, "Bioimaging: second window for in vivo imaging," *Nature nanotechnology*, vol. 4, no. 11, pp. 710–711, 2009.

[24] M.-F. Tsai, S.-H. G. Chang, F.-Y. Cheng, V. Shanmugam, Y.-S. Cheng, C.-H. Su, and C.-S. Yeh, "Au nanorod design as light-absorber in the first and second biological near-infrared windows for in vivo photothermal therapy," *ACS nano*, vol. 7, no. 6, pp. 5330–5342, 2013.

[25] E. Pop, D. Mann, Q. Wang, K. Goodson, and H. Dai, "Thermal conductance of an individual single-wall carbon nanotube above room temperature," *Nano letters*, vol. 6, no. 1, pp. 96–100, 2006.

[26] L. V. Wang and H.-i. Wu, *Biomedical optics: principles and imaging*. John Wiley & Sons, 2012.

[27] R. G. Gould *et al.*, "The laser, light amplification by stimulated emission of radiation," in *The Ann Arbor conference on optical pumping, the University of Michigan*, vol. 15, p. 128, 1959.

[28] P. Beard, "Biomedical photoacoustic imaging," *Interface Focus*, vol. 1, no. 4, pp. 602–631, 2011.

[29] A. Rosencwaig, "Photoacoustic spectroscopy of solids," *The Journal of the Acoustical Society of America*, vol. 58, no. S1, pp. S52–S52, 1975.

[30] A. Taylor, S. Branch, H. Crews, and D. Halls, "Photoacoustic spectroscopy, applications," *Chemistry*, vol. 62, no. 78R, p. 84R, 1999.

[31] V. Spagnolo, P. Patimisco, S. Borri, G. Scamarcio, B. E. Bernacki, and J. Kriesel, "Part-per-trillion level sf 6 detection using a quartz enhanced photoacoustic spectroscopy-based sensor with single-mode fiber-coupled quantum cascade laser excitation," *Optics letters*, vol. 37, no. 21, pp. 4461–4463, 2012.

[32] J. Valvano, J. Cochran, and K. Diller, "Thermal conductivity and diffusivity of biomaterials measured with self-heated thermistors," *International Journal of Thermophysics*, vol. 6, no. 3, pp. 301–311, 1985.

[33] J. Lu, H. Ying, Z. Sun, M. Motamedi, B. Bell, and L. Sheppard, "In vitro measurement of speed of sound during coagulate tissue heating," in *Ultrasonics Symposium, 1996. Proceedings., 1996 IEEE*, vol. 2, pp. 1299–1302, IEEE, 1996.

[34] K. Brugger and T. Fritz, "Grüneisen gamma from elastic data," *Physical Review*, vol. 157, no. 3, p. 524, 1967.

[35] M. W. Sigrist, "Laser generation of acoustic waves in liquids and gases," *Journal of applied physics*, vol. 60, no. 7, pp. R83–R122, 1986.

[36] S. A. Ermilov, T. Khamapirad, A. Conjusteau, M. H. Leonard, R. Lacewell, K. Mehta, T. Miller, and A. A. Oraevsky, "Laser optoacoustic imaging system for detection of breast cancer," *Journal of biomedical optics*, vol. 14, no. 2, p. 024007, 2009.

[37] G. Diebold and T. Sun, "Properties of photoacoustic waves in one, two, and three dimensions," *Acta Acustica united with Acustica*, vol. 80, no. 4, pp. 339–351, 1994.

[38] H. F. Zhang, K. Maslov, M. Sivaramakrishnan, G. Stoica, and L. V. Wang, "Imaging of hemoglobin oxygen saturation variations in single vessels in vivo using photoacoustic microscopy," *Applied physics letters*, vol. 90, no. 5, p. 053901, 2007.

[39] X. Wang, X. Xie, G. Ku, L. V. Wang, and G. Stoica, "Noninvasive imaging of hemoglobin concentration and oxygenation in the rat brain using high-resolution photoacoustic tomography," *Journal of biomedical optics*, vol. 11, no. 2, p. 024015, 2006.

[40] K. Maslov, H. F. Zhang, and L. V. Wang, "Effects of wavelength-dependent fluence attenuation on the noninvasive photoacoustic imaging of hemoglobin oxygen saturation in subcutaneous vasculature in vivo," *Inverse Problems*, vol. 23, no. 6, p. S113, 2007.

[41] O. M. L. C. Scott Prahl, "Optical absorption of hemoglobin," 1999.

[42] G. M. Hale and M. R. Querry, "Optical constants of water in the 200-nm to 200-μm wavelength region," *Applied optics*, vol. 12, no. 3, pp. 555–563, 1973.

[43] S. Manohar, S. E. Vaartjes, J. C. van Hespen, J. M. Klaase, F. M. van den Engh, W. Steenbergen, and T. G. Van Leeuwen, "Initial results of in vivo non-invasive cancer imaging in the human breast using near-infrared photoacoustics," *Optics express*, vol. 15, no. 19, pp. 12277–12285, 2007.

[44] T. J. Allen and P. C. Beard, "Pulsed near-infrared laser diode excitation system for biomedical photoacoustic imaging," *Optics letters*, vol. 31, no. 23, pp. 3462–3464, 2006.

[45] G. S. Filonov, A. Krumholz, J. Xia, J. Yao, L. V. Wang, and V. V. Verkhusha, "Deep-tissue photoacoustic tomography of a genetically encoded near-infrared fluorescent probe," *Angewandte Chemie International Edition*, vol. 51, no. 6, pp. 1448–1451, 2012.

[46] J. Laufer, D. Delpy, C. Elwell, and P. Beard, "Quantitative spatially resolved measurement of tissue chromophore concentrations using photoacoustic spectroscopy: application to the measurement of blood oxygenation and haemoglobin concentration," *Physics in Medicine & Biology*, vol. 52, no. 1, p. 141, 2006.

[47] Z. Xu, C. Li, and L. V. Wang, "Photoacoustic tomography of water in phantoms and tissue," *Journal of biomedical optics*, vol. 15, no. 3, p. 036019, 2010.

[48] J. Laufer, C. Elwell, D. Delpy, and P. Beard, "In vitro measurements of absolute blood oxygen saturation using pulsed near-infrared photoacoustic spectroscopy: accuracy and resolution," *Physics in Medicine & Biology*, vol. 50, no. 18, p. 4409, 2005.

[49] K. Maslov, G. Stoica, and L. V. Wang, "In vivo dark-field reflection-mode photoacoustic microscopy," *Optics letters*, vol. 30, no. 6, pp. 625–627, 2005.

[50] H. F. Zhang, K. Maslov, G. Stoica, and L. V. Wang, "Functional photoacoustic microscopy for high-resolution and noninvasive in vivo imaging," *Nature biotechnology*, vol. 24, no. 7, p. 848, 2006.

[51] C. P. Favazza, L. V. Wang, and L. A. Cornelius, "In vivo functional photoacoustic microscopy of cutaneous microvasculature in human skin," *Journal of biomedical optics*, vol. 16, no. 2, p. 026004, 2011.

[52] S. Park, C. Lee, J. Kim, and C. Kim, "Acoustic resolution photoacoustic microscopy," *Biomedical Engineering Letters*, vol. 4, no. 3, pp. 213–222, 2014.

[53] K. Maslov, H. F. Zhang, S. Hu, and L. V. Wang, "Optical-resolution photoacoustic microscopy for in vivo imaging of single capillaries," *Optics letters*, vol. 33, no. 9, pp. 929–931, 2008.

[54] S. Iijima, "Helical microtubules of graphitic carbon," *nature*, vol. 354, no. 6348, p. 56, 1991.

[55] A. K. Geim and K. S. Novoselov, "The rise of graphene," *Nature materials*, vol. 6, no. 3, p. 183, 2007.

[56] K. S. Novoselov, A. K. Geim, S. V. Morozov, D. Jiang, Y. Zhang, S. V. Dubonos, I. V. Grigorieva, and A. A. Firsov, "Electric field effect in atomically thin carbon films," *science*, vol. 306, no. 5696, pp. 666–669, 2004.

[57] R. Saito, G. Dresselhaus, and M. S. Dresselhaus, *Physical properties of carbon nanotubes*. World Scientific, 1998.

[58] P. R. Wallace, "The band theory of graphite," *Physical Review*, vol. 71, no. 9, p. 622, 1947.

[59] X. Tu, S. Manohar, A. Jagota, and M. Zheng, "Dna sequence motifs for structure-specific recognition and separation of carbon nanotubes," *Nature*, vol. 460, no. 7252, pp. 250–253, 2009.

[60] H. Sun, G. Ge, J. Zhu, H. Yan, Y. Lu, Y. Wu, J. Wan, M. Han, and Y. Luo, "High electrical conductivity of graphene-based transparent conductive films with silver nanocomposites," *RSC Advances*, vol. 5, no. 130, pp. 108044–108049, 2015.

[61] K. Kostarelos, A. Bianco, and M. Prato, "Promises, facts and challenges for carbon nanotubes in imaging and therapeutics," *Nature nanotechnology*, vol. 4, no. 10, p. 627, 2009.

[62] E. B. Malarkey, K. A. Fisher, E. Bekyarova, W. Liu, R. C. Haddon, and V. Parpura, "Conductive single-walled carbon nanotube substrates modulate neuronal growth," *Nano letters*, vol. 9, no. 1, pp. 264–268, 2008.

[63] Z. Liu, S. Tabakman, K. Welsher, and H. Dai, "Carbon nanotubes in biology and medicine: in vitro and in vivo detection, imaging and drug delivery," *Nano research*, vol. 2, no. 2, pp. 85–120, 2009.

[64] F. Zhou, X. Da, Z. Ou, B. Wu, D. E. Resasco, and W. R. Chen, "Cancer photothermal therapy in the near-infrared region by using single-walled carbon nanotubes," *Journal of biomedical optics*, vol. 14, no. 2, p. 021009, 2009.

[65] X. Liu, H. Tao, K. Yang, S. Zhang, S.-T. Lee, and Z. Liu, "Optimization of surface chemistry on single-walled carbon nanotubes for in vivo photothermal ablation of tumors," *Biomaterials*, vol. 32, no. 1, pp. 144–151, 2011.

[66] Z. Liu, K. Chen, C. Davis, S. Sherlock, Q. Cao, X. Chen, and H. Dai, "Drug delivery with carbon nanotubes for in vivo cancer treatment," *Cancer research*, vol. 68, no. 16, pp. 6652–6660, 2008.

[67] K. Welsher, Z. Liu, S. P. Sherlock, J. T. Robinson, Z. Chen, D. Daranciang, and H. Dai, "A route to brightly fluorescent carbon nanotubes for near-infrared imaging in mice," *Nature nanotechnology*, vol. 4, no. 11, p. 773, 2009.

[68] C. Zavaleta, A. De La Zerda, Z. Liu, S. Keren, Z. Cheng, M. Schipper, X. Chen, H. Dai, and S. Gambhir, "Noninvasive raman spectroscopy in living mice for evaluation of tumor targeting with carbon nanotubes," *Nano letters*, vol. 8, no. 9, pp. 2800–2805, 2008.

[69] B. S. Harrison and A. Atala, "Carbon nanotube applications for tissue engineering," *Biomaterials*, vol. 28, no. 2, pp. 344–353, 2007.

[70] C. Richard, B.-T. Doan, J.-C. Beloeil, M. Bessodes, É. Tóth, and D. Scherman, "Noncovalent functionalization of carbon nanotubes with amphiphilic gd3+ chelates: toward powerful t1 and t2 mri contrast agents," *Nano letters*, vol. 8, no. 1, pp. 232–236, 2008.

[71] L. G. Delogu, G. Vidili, E. Venturelli, C. Ménard-Moyon, M. A. Zoroddu, G. Pilo, P. Nicolussi, C. Ligios, D. Bedognetti, F. Sgarrella, *et al.*, "Functionalized multiwalled carbon nanotubes as ultrasound contrast agents," *Proceedings of the National Academy of Sciences*, vol. 109, no. 41, pp. 16612–16617, 2012.

[72] L. Lacerda, A. Soundararajan, R. Singh, G. Pastorin, K. T. Al-Jamal, J. Turton, P. Frederik, M. A. Herrero, S. Li, A. Bao, *et al.*, "Dynamic imaging of functionalized multi-walled carbon nanotube systemic circulation and urinary excretion," *Advanced Materials*, vol. 20, no. 2, pp. 225–230, 2008.

[73] L. P. Zanello, B. Zhao, H. Hu, and R. C. Haddon, "Bone cell proliferation on carbon nanotubes," *Nano letters*, vol. 6, no. 3, pp. 562–567, 2006.

[74] K. Sahithi, M. Swetha, K. Ramasamy, N. Srinivasan, and N. Selvamurugan, "Polymeric composites containing carbon nanotubes for bone tissue engineering," *International journal of biological macromolecules*, vol. 46, no. 3, pp. 281–283, 2010.

[75] L. Pan, X. Pei, R. He, Q. Wan, and J. Wang, "Multiwall carbon nanotubes/polycaprolactone composites for bone tissue engineering application," *Colloids and Surfaces B: Biointerfaces*, vol. 93, pp. 226–234, 2012.

[76] J. Foroughi, G. M. Spinks, G. G. Wallace, J. Oh, M. E. Kozlov, S. Fang, T. Mirfakhrai, J. D. Madden, M. K. Shin, S. J. Kim, *et al.*, "Torsional carbon nanotube artificial muscles," *Science*, vol. 334, no. 6055, pp. 494–497, 2011.

[77] S. Beg, M. Rizwan, A. M. Sheikh, M. S. Hasnain, K. Anwer, and K. Kohli, "Advancement in carbon nanotubes: basics, biomedical applications and toxicity," *Journal of pharmacy and pharmacology*, vol. 63, no. 2, pp. 141–163, 2011.

[78] J. Wang and M. Musameh, "Carbon-nanotubes doped polypyrrole glucose biosensor," *Analytica Chimica Acta*, vol. 539, no. 1-2, pp. 209–213, 2005.

[79] A. D. Maynard, P. A. Baron, M. Foley, A. A. Shvedova, E. R. Kisin, and V. Castranova, "Exposure to carbon nanotube material: aerosol release during the handling of unrefined single-walled carbon nanotube material," *Journal of Toxicology and Environmental Health, Part A*, vol. 67, no. 1, pp. 87–107, 2004.

[80] M. Foldvari and M. Bagonluri, "Carbon nanotubes as functional excipients for nanomedicines: Ii. drug delivery and biocompatibility issues," *Nanomedicine: Nanotechnology, Biology and Medicine*, vol. 4, no. 3, pp. 183–200, 2008.

[81] R. Singh, D. Pantarotto, L. Lacerda, G. Pastorin, C. Klumpp, M. Prato, A. Bianco, and K. Kostarelos, "Tissue biodistribution and blood clearance rates

of intravenously administered carbon nanotube radiotracers," *Proceedings of the National Academy of Sciences*, vol. 103, no. 9, pp. 3357–3362, 2006.

[82] D. Pantarotto, R. Singh, D. McCarthy, M. Erhardt, J.-P. Briand, M. Prato, K. Kostarelos, and A. Bianco, "Functionalized carbon nanotubes for plasmid dna gene delivery," *Angewandte Chemie International Edition*, vol. 43, no. 39, pp. 5242–5246, 2004.

[83] K. E. Geckeler and T. Premkumar, "Carbon nanotubes: are they dispersed or dissolved in liquids?," *Nanoscale research letters*, vol. 6, no. 1, p. 136, 2011.

[84] S. D. Bergin, V. Nicolosi, P. V. Streich, S. Giordani, Z. Sun, A. H. Windle, P. Ryan, N. P. P. Niraj, Z.-T. T. Wang, L. Carpenter, *et al.*, "Towards solutions of single-walled carbon nanotubes in common solvents," *Advanced Materials*, vol. 20, no. 10, pp. 1876–1881, 2008.

[85] V. A. Davis, A. N. G. Parra-Vasquez, M. J. Green, P. K. Rai, N. Behabtu, V. Prieto, R. D. Booker, J. Schmidt, E. Kesselman, W. Zhou, *et al.*, "True solutions of single-walled carbon nanotubes for assembly into macroscopic materials.," *Nature nanotechnology*, vol. 4, no. 12, 2009.

[86] A. Nish, J.-Y. Hwang, J. Doig, and R. J. Nicholas, "Highly selective dispersion of single-walled carbon nanotubes using aromatic polymers," *Nature nanotechnology*, vol. 2, no. 10, p. 640, 2007.

[87] M. Bottini, N. Rosato, and N. Bottini, "Peg-modified carbon nanotubes in biomedicine: current status and challenges ahead," *Biomacromolecules*, vol. 12, no. 10, pp. 3381–3393, 2011.

[88] S. Siregar, S. Oktamuliani, and Y. Saijo, "A theoretical model of laser heating carbon nanotubes," *Nanomaterials*, vol. 8, no. 8, 2018.

[89] S. Siregar, I. U. Haq, R. Nagaoka, and Y. Saijo, "Application of single walled carbon nanotubes for heating agent in photothermal therapy," *arXiv preprint arXiv:1611.08094*, 2016.

[90] L. O. Svaasand, C. J. Gomer, and E. Morinelli, "On the physical rationale of laser induced hyperthermia," *Lasers in Medical Science*, vol. 5, no. 2, pp. 121–128, 1990.

[91] X. Huang, P. K. Jain, I. H. El-Sayed, and M. A. El-Sayed, "Plasmonic photothermal therapy (pptt) using gold nanoparticles," *Lasers in medical science*, vol. 23, no. 3, pp. 217–228, 2008.

[92] L. Shen and J. Li, "Transversely isotropic elastic properties of single-walled carbon nanotubes," *Physical Review B*, vol. 69, no. 4, p. 045414, 2004.

[93] A. Aqel, K. M. A. El-Nour, R. A. Ammar, and A. Al-Warthan, "Carbon nanotubes, science and technology part (i) structure, synthesis and characterisation," *Arabian Journal of Chemistry*, vol. 5, no. 1, pp. 1–23, 2012.

[94] T. E. Cooper and G. J. Trezek, "A probe technique for determining the thermal conductivity of tissue," *Journal of Heat Transfer*, vol. 94, no. 2, pp. 133–140, 1972.

[95] M. Haque, C. Marinelli, F. Udrea, and W. Milne, "Absorption characteristics of single wall carbon nanotubes," *NSTI Nanotech (Boston, MA)*, 2006.

[96] Z. Qin and J. C. Bischof, "Thermophysical and biological responses of gold nanoparticle laser heating," *Chemical Society Reviews*, vol. 41, no. 3, pp. 1191–1217, 2012.

[97] A. E. Cerussi, N. S. Shah, D. Hsiang, A. Durkin, J. A. Butler, and B. J. Tromberg, "In vivo absorption, scattering, and physiologic properties of 58 malignant breast tumors determined by broadband diffuse optical spectroscopy," *Journal of biomedical optics*, vol. 11, no. 4, p. 044005, 2006.

[98] J. Xie, S. Lee, and X. Chen, "Nanoparticle-based theranostic agents," *Advanced drug delivery reviews*, vol. 62, no. 11, pp. 1064–1079, 2010.

[99] S. Del Vecchio, A. Zannetti, R. Fonti, L. Pace, and M. Salvatore, "Nuclear imaging in cancer theranostics," *The Quarterly Journal of Nuclear Medicine and Molecular Imaging*, vol. 51, no. 2, p. 152, 2007.

[100] K. Yang, L. Feng, X. Shi, and Z. Liu, "Nano-graphene in biomedicine: theranostic applications," *Chemical Society Reviews*, vol. 42, no. 2, pp. 530–547, 2013.

[101] N. Ahmed, H. Fessi, and A. Elaissari, "Theranostic applications of nanoparticles in cancer," *Drug discovery today*, vol. 17, no. 17-18, pp. 928–934, 2012.

[102] S. Siregar, R. Nagaoka, I. U. Haq, and Y. Saijo, "Non local means denoising in photoacoustic imaging," *Japanese Journal of Applied Physics*, vol. 57, no. 7S1, p. 07LB06, 2018.

[103] S. Manohar, R. G. Willemink, F. van der Heijden, C. H. Slump, and T. G. van Leeuwen, "Concomitant speed-of-sound tomography in photoacoustic imaging," *Applied physics letters*, vol. 91, no. 13, p. 131911, 2007.

[104] R. J. Zemp, R. Bitton, K. K. Shung, M.-L. Li, G. Stoica, and L. V. Wang, "Photoacoustic imaging of the microvasculature with a high-frequency ultrasound array transducer," *Journal of biomedical optics*, vol. 12, no. 1, p. 010501, 2007.

[105] A. Manninen, J. Sand, J. Saarela, T. Sorvajärvi, J. Toivonen, and R. Hernberg, "Electromechanical film as a photoacoustic transducer," *Optics Express*, vol. 17, no. 19, pp. 16994–16999, 2009.

[106] E. R. Hill, W. Xia, M. J. Clarkson, and A. E. Desjardins, "Identification and removal of laser-induced noise in photoacoustic imaging using singular value decomposition," *Biomedical optics express*, vol. 8, no. 1, pp. 68–77, 2017.

[107] A. Buades, B. Coll, and J.-M. Morel, "Non-local means denoising," *Image Processing On Line*, vol. 1, pp. 208–212, 2011.

[108] A. Buades, B. Coll, and J.-M. Morel, "A non-local algorithm for image denoising," in *Computer Vision and Pattern Recognition, 2005. CVPR 2005. IEEE Computer Society Conference on*, vol. 2, pp. 60–65, IEEE, 2005.

[109] J. Salmon, "On two parameters for denoising with non-local means," *IEEE Signal Processing Letters*, vol. 17, no. 3, pp. 269–272, 2010.

[110] J. V. Manjón, J. Carbonell-Caballero, J. J. Lull, G. García-Martí, L. Martí-Bonmatí, and M. Robles, "Mri denoising using non-local means," *Medical image analysis*, vol. 12, no. 4, pp. 514–523, 2008.

[111] J. V. Manjón, P. Coupé, L. Martí-Bonmatí, D. L. Collins, and M. Robles, "Adaptive non-local means denoising of mr images with spatially varying noise levels," *Journal of Magnetic Resonance Imaging*, vol. 31, no. 1, pp. 192–203, 2010.

[112] P. Coupé, P. Yger, and C. Barillot, "Fast non local means denoising for 3d mr images," in *International Conference on Medical Image Computing and Computer-Assisted Intervention*, pp. 33–40, Springer, 2006.

[113] P. Coupé, P. Hellier, C. Kervrann, and C. Barillot, "Nonlocal means-based speckle filtering for ultrasound images," *IEEE transactions on image processing*, vol. 18, no. 10, pp. 2221–2229, 2009.

[114] F. P. X. De Fontes, G. A. Barroso, P. Coupé, and P. Hellier, "Real time ultrasound image denoising," *Journal of real-time image processing*, vol. 6, no. 1, pp. 15–22, 2011.

[115] C. Chan, R. Fulton, D. D. Feng, and S. Meikle, "Median non-local means filtering for low snr image denoising: Application to pet with anatomical knowledge," in *Nuclear Science Symposium Conference Record (NSS/MIC), 2010 IEEE*, pp. 3613–3618, IEEE, 2010.

[116] J. Dutta, R. M. Leahy, and Q. Li, "Non-local means denoising of dynamic pet images," *PloS one*, vol. 8, no. 12, p. e81390, 2013.

[117] Z. Li, L. Yu, J. D. Trzasko, D. S. Lake, D. J. Blezek, J. G. Fletcher, C. H. McCollough, and A. Manduca, "Adaptive nonlocal means filtering based on local noise level for ct denoising," *Medical physics*, vol. 41, no. 1, 2014.

[118] Y. Chen, Z. Yang, Y. Hu, G. Yang, Y. Zhu, Y. Li, W. Chen, C. Toumoulin, *et al.*, "Thoracic low-dose ct image processing using an artifact suppressed large-scale nonlocal means," *Physics in Medicine & Biology*, vol. 57, no. 9, p. 2667, 2012.

[119] S. V. d. Walt, S. C. Colbert, and G. Varoquaux, "The numpy array: a structure for efficient numerical computation," *Computing in Science & Engineering*, vol. 13, no. 2, pp. 22–30, 2011.

[120] F. Pedregosa, G. Varoquaux, A. Gramfort, V. Michel, B. Thirion, O. Grisel, M. Blondel, P. Prettenhofer, R. Weiss, V. Dubourg, J. Vanderplas, A. Passos, D. Cournapeau, M. Brucher, M. Perrot, and E. Duchesnay, "Scikit-learn: Machine learning in Python," *Journal of Machine Learning Research*, vol. 12, pp. 2825–2830, 2011.

[121] S. Van der Walt, J. L. Schönberger, J. Nunez-Iglesias, F. Boulogne, J. D. Warner, N. Yager, E. Gouillart, and T. Yu, "scikit-image: image processing in python," *PeerJ*, vol. 2, p. e453, 2014.

[122] J. D. Hunter, "Matplotlib: A 2d graphics environment," *Computing in science & engineering*, vol. 9, no. 3, pp. 90–95, 2007.

[123] N. Otsu, "A threshold selection method from gray-level histograms," *IEEE transactions on systems, man, and cybernetics*, vol. 9, no. 1, pp. 62–66, 1979.

[124] J. Mairal, F. Bach, J. Ponce, and G. Sapiro, "Online dictionary learning for sparse coding," in *Proceedings of the 26th annual international conference on machine learning*, pp. 689–696, ACM, 2009.

[125] E. M. Eksioglu, "Online dictionary learning algorithm with periodic updates and its application to image denoising," *Expert Systems with Applications*, vol. 41, no. 8, pp. 3682–3690, 2014.

[126] S. Ravishankar and Y. Bresler, "Mr image reconstruction from highly undersampled k-space data by dictionary learning," *IEEE transactions on medical imaging*, vol. 30, no. 5, pp. 1028–1041, 2011.

[127] J. Caballero, A. N. Price, D. Rueckert, and J. V. Hajnal, "Dictionary learning and time sparsity for dynamic mr data reconstruction," *IEEE transactions on medical imaging*, vol. 33, no. 4, pp. 979–994, 2014.

[128] Y. Song, Z. Zhu, Y. Lu, Q. Liu, and J. Zhao, "Reconstruction of magnetic resonance imaging by three-dimensional dual-dictionary learning," *Magnetic resonance in medicine*, vol. 71, no. 3, pp. 1285–1298, 2014.

[129] Y. Chen, L. Shi, Q. Feng, J. Yang, H. Shu, L. Luo, J.-L. Coatrieux, and W. Chen, "Artifact suppressed dictionary learning for low-dose ct image processing," *IEEE transactions on medical imaging*, vol. 33, no. 12, pp. 2271–2292, 2014.

[130] Q. Xu, H. Yu, X. Mou, L. Zhang, J. Hsieh, and G. Wang, "Low-dose x-ray ct reconstruction via dictionary learning," *IEEE Transactions on Medical Imaging*, vol. 31, no. 9, pp. 1682–1697, 2012.

[131] Y. Chen, X. Yin, L. Shi, H. Shu, L. Luo, J.-L. Coatrieux, and C. Toumoulin, "Improving abdomen tumor low-dose ct images using a fast dictionary learning based processing," *Physics in Medicine & Biology*, vol. 58, no. 16, p. 5803, 2013.

[132] I. Tošić, I. Jovanović, P. Frossard, M. Vetterli, and N. Durić, "Ultrasound tomography with learned dictionaries," in *Acoustics Speech and Signal Processing (ICASSP), 2010 IEEE International Conference on*, pp. 5502–5505, IEEE, 2010.

[133] M. Aharon, M. Elad, and A. Bruckstein, "*rmk*-svd: An algorithm for designing overcomplete dictionaries for sparse representation," *IEEE Transactions on signal processing*, vol. 54, no. 11, pp. 4311–4322, 2006.

Publication list

Doctoral Program, Graduate School of Biomedical Engineering, Tohoku University

1. **S. Siregar**, S. Oktamuliani, and Y. Saijo,"A theoretical model of laser heating carbon nanotubes," *Nanomaterials* vol. 8, no. 8, 2018.

2. **S. Siregar**, R. Nagaoka, I. U. Haq, and Y. Saijo, "Non local means denoising in photoacoustic imaging," *Japanese Journal of Applied Physics* vol. 57, no. 7S1, p. 07LB06, 2018.

3. **S. Siregar**, Ryo Nagaoka, K. Ishikawa, Y. Saijo, "Carbon nanotubes as potential candidate for photoacoustic imaging contrast agent," *Proceedings of Meetings on Acoustics* 6ICU. vol. 32, p. 020018, ASA, 2017.

4. I. U. Haq, **S. Siregar**, R. Nagaoka and Y. Saijo, "Vascular Bifurcation Detection by Symmetric Analysis of Eigenvalues," *IET Conference Proceedings*, p. 30, 2017.

5. I. U. Haq, R. Nagaoka, **S. Siregar** and Y. Saijo. "Sparse-representation-based denoising of photoacoustic images," *Biomedical Physics & Engineering Express*, vol. 3, no. 4, 045014, 2017.

Master Program, Graduate School of Science, Tohoku University

1. R. Saito, A.R.T. Nugraha, E.H. Hasdeo, **S. Siregar**, H. Guo, and T. Yang,"Ultraviolet Raman spectroscopy of graphene and transition metal dichalcogenides," *Physica Status Solidi (b)* vol. 252, no. 11, pp. 2363-2374, 2015.

2. H. Liu, **S. Siregar**, E. H. Hasdeo, Y. Kumamoto, C. Shen, C. Cheng, L. Li, R. Saito, and S. Kawata, "Deep-ultraviolet Raman scattering studies of monolayer graphene thin films," *Carbon* vol. 81, pp. 807-813, 2015.

Undergraduate Program, Department of Physics, Universitas Indonesia

1. M. A. Majidi, **S. Siregar**, and A. Rusydi, "Theoretical study of optical conductivity of graphene with magnetic and nonmagnetic adatoms," *Physical Review B*, vol. 90, no. 19, p. 195442, 2014.